Wavefront Microscopy Using Quadriwave Lateral Shearing Interferometry: From Bioimaging to Nanophotonics

Guillaume Baffou

Wavefront microscopy using quadriwave lateral shearing interferometry: from bioimaging to nanophotonics

GUILLAUME BAFFOU[1,*]

[1] Institut Fresnel, CNRS, Aix-Marseille Université, Centrale Marseille, Marseille, France
[*] guillaume.baffou@fresnel.fr

Compiled February 16, 2023

Common cameras are only sensitive to the intensity of light, discarding an essential feature of a light wave: its phase profile, or equivalently, its wavefront profile. This Review focuses on a rising wavefront imaging technique called quadriwave lateral shearing interferometry (QLSI), based on the simple use of a 2-dimensional diffraction grating, aka a cross-grating, in front of a regular camera. We detail the working principle of QLSI and its implementation on an optical microscope. We highlight its microscopy applications in bioimaging and nanophotonics, in particular for the characterization of living cells, nanoparticles, 2D-materials, metasurfaces, microscale temperature gradients and surface topography. Finally, we draw a critical comparison of QLSI with current quantitative phase microscopy techniques, namely DHM, SLIM and DPM.

Quantitative phase microscopy (QPM) designates a family of optical microscopy techniques aimed at mapping the phase of a light beam after crossing the object plane of a microscope [1, 2]. Fueled by the development of CCD sensors and computational progress, a large variety of high-resolution, full-field QPM techniques emerged since the 90s, based on much different experimental configurations, but all based on the same concept: using interferences to convert the phase information into intensity, detectable by cameras. Among the most popular QPM techniques, let us cite digital holography microscopy (DHM) [3, 4], DPM (diffraction phase microscopy) [5, 6] and spatial light interference microscopy (SLIM) [7, 8]. QPMs found important applications in biology, to image cells in culture. Cells are mostly transparent, but they can imprint a phase shift to a light beam leading to QPM images with much higher contrast than intensity images. Moreover, the refractive index of a biological cell being directly related to its mass density, QPMs have the ability to map the bio-mass spatial density of biological samples [9, 10]. In recent years, QPM has emerged as a serious complementary approach to the flourishing field of fluorescence microscopy in bioimaging.

Quadriwave lateral shearing interferometry (QLSI) is an optical wavefront imaging technique based on the use of a 2-dimensional grating in front of a camera.[11, 12] When implemented on a microscope, QLSI can be used as a QPM because of the equivalence between phase and wavefront. QLSI is currently attracting substantial attention because of its increasingly active use in microscopy, and because it gathers several important benefits in terms of simplicity (a grating in front of a camera), sensitivity, spatial resolution and insensitivity to environmental perturbation.

This review focuses on QLSI, from the fundamentals to its applications. The first part introduces the concepts of phase and wavefront in optics, and how they can be mapped. The second part focuses on QLSI and its working principle. The third part introduces the implementation of QLSI in microscopy, a modality that we recently proposed to name cross-grating wavefront microscopy (CGM), and review the applications of CGM in biology, nanophotonics and surface topography. The last part compares CGM with QPMs, namely DHM, DPM and SLIM, for applications in biology.

1. OPTICAL WAVEFRONT AND PHASE IMAGING

A. Definition of W and φ

Optical wavefronts are surfaces connecting points of a light wave with the same phase. Wavefronts are locally perpendicular to wave vectors $\mathbf{k}$, i.e., perpendicular to the direction of wave propagation. The wavefront profile W impinging on a planar sensor is defined as in Fig. 1. On this sensor, the phase profile φ of the light beam is proportional to W, according to the relation:

$$\varphi = \frac{2\pi}{\lambda} W \tag{1}$$

where λ is the wavelength of light. This equation involves approximations. The arbitrary additional phase constant, depending on the chosen origin of phase, has been set to zero for the sake of simplicity, and a monochromatic light is considered. We also

consider weakly diverging beams, which is a valid approximation when considering the wavefront impinging on the camera sensor of a high-magnification microscope. The use of a single wavefront also implies a scalar approximation. For polarized light, one has to define two different wavefronts corresponding to two orthogonal polarization directions.

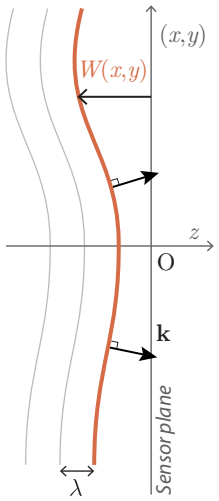

Fig. 1. Schematic of a light wavefront impinging on a sensor. W is the wavefront profile, λ the wavelength in vacuum and $\mathbf{k}$ the wave vector.

B. Imaging W and φ

The electric field amplitude impinging on the sensor, in the scalar approximation, reads

$$A = \sqrt{I}\exp\left(-ikW\right) = \sqrt{I}\exp\left(-i\varphi\right) \tag{2}$$

where $k = 2\pi/\lambda$. When using conventional cameras, one only accesses the intensity of light $|A|^2 = I$.

To access W or φ, one has to make this beam interfere with another. The so-called off-axis approach consists in making A interfere with a reference light beam A_R propagating along a tilted direction $\mathbf{k}_\mathrm{R}$ (Fig. 2a), so that the intensity I_c measured on the camera plane contains information related to φ:[1]

$$\begin{aligned} I_\mathrm{c}(x,y) &= |A(x,y) + A_\mathrm{R}|^2 \\ &= I(x,y) + I_\mathrm{R} + 2\sqrt{I(x,y)I_\mathrm{R}}\cos\left[\mathbf{k}_\mathrm{R}\cdot\mathbf{r} + \varphi(x,y))\right]. \end{aligned} \tag{3}$$

The image produced on the camera, called an interferogram, displays fringes stemming from the term $\mathbf{k}_\mathrm{R}\cdot\mathbf{r}$ in the cosine. Using a demodulation algorithm around the spatial frequency of the fringes, the phase profile φ can be retrieved. This off-axis configuration is at the basis of several QPMs, such as DHM and DPM. There exist other approaches to measure phase profile (such a phase-shifting methods). We chose here to present only the off-axis configuration because it is a popular one, and because an educational and instructive comparison can be made with QLSI, as shown hereinafter.

In off-axis lateral shearing interferometry (LSI), the beam of interest interferes with a replica of itself that is both slightly tilted and shifted (Fig. 2b). The resulted intensity profile measured by the sensor reads thus[12]

$$\begin{aligned} I_\mathrm{c}(x,y) &= I(x,y) + I(x+a,y) \\ &+ 2\sqrt{I(x+a,y)I(x,y)}\cos[\underbrace{\mathbf{k}_\mathrm{R}\cdot\mathbf{r}}_{\text{tilt}} + \underbrace{\varphi(x+a,y) - \varphi(x,y)}_{\substack{\text{shift} \\ = a\partial_x\varphi}}]. \end{aligned} \tag{4}$$

Importantly, in LSI, both the tilt and the lateral shift of the beam are important: the tilt creates the fringes and the shift embeds information on the phase or wavefront gradient, no longer on the phase itself like in off-axis interferometry (Eq. 3).

The last instructive imaging technique that we shall present is Shack-Hartmann (SH) wavefront sensing. SH wavefront sensing is based on the implementation of an array of micro-lenses (called lenslets) in front of a camera [13, 14]. When a light beam is sampled by the lenslet array, it gives rise to an array of bright spots in its focal plane where a camera is located (Fig. 2c). The displacements of these spots are proportional to the local slope (i.e. gradient) of the wavefront [13, 14], and their monitoring enables the reconstruction of the wavefront gradient profile. Proposed in 1971 by Shack and Platt [15], such a simple design can thus map the wavefront gradient of a light beam. The main limitation of SH wavefront sensing is its poor spatial sampling (i.e., poor spatial resolution) limited by the lenslet size (between 100 and 300 µm), which provides images of typically 100×100 pixels, while common cameras rather feature a pixel size of 10 µm. The consequence is that SH wavefront sensors can only render the low frequencies of a wavefront. Such a limitation makes SH wavefront sensors mostly suited for the study of optical aberrations, where wavefront distortions are particularly smooth and do not possess high spatial frequencies. So far, the applications of SH wavefront sensing have been in optics and laser metrology [16], ophthalmology [17] and adaptive optics systems for astronomy [18, 19]. There exist other wavefront imaging techniques.[20–24] We focus only here on SH wavefront sensing because it is very popular, and because there is a close relation with QLSI that we shall explain in the next section.

2. QUADRIWAVE LATERAL SHEARING INTERFEROMETRY (QLSI)

Quadriwave lateral shearing interferometry (QLSI) is a high-definition wavefront imaging technique, invented and patented by Primot et al. in 2000 (Fig. 3b) [11, 12]. It is based on the LSI principle (Fig. 2b) where two waves interfere along each crossed directions of space, say x and y (4 waves in total), and where these 4 waves are generated by the 4 first diffraction orders of a specific 2-dimensional grating placed at a millimetric distance from a camera sensor (Fig. 3a). The unit cell of this specific gross-grating, of dimension $\Gamma \times \Gamma$, is designed to cancel other orders than ± 1. It consists of black (opaque) crossed lines, $\Gamma/6$ in width (which cancels the orders ± 3 and ± 5), defining transparent square holes on which a checkerboard $0 - \pi$ pattern was imprinted (which cancels even diffraction orders: 0, ± 2, ± 4, etc). This diffractive element is usually called a Modified Hartmann Mask (MHM), for historical reasons. Since a MHM is nothing but a 2D-grating, working as a grating, used as a grating, I rather recommend to refer to it as a 2D-grating (or "cross-grating" that is a synonym[25]), rather than a mask, for the sake of simplicity and clarity.

As a result, the incident beam is reproduced in 4 replicas that propagate along slightly shifted directions and that interfere on

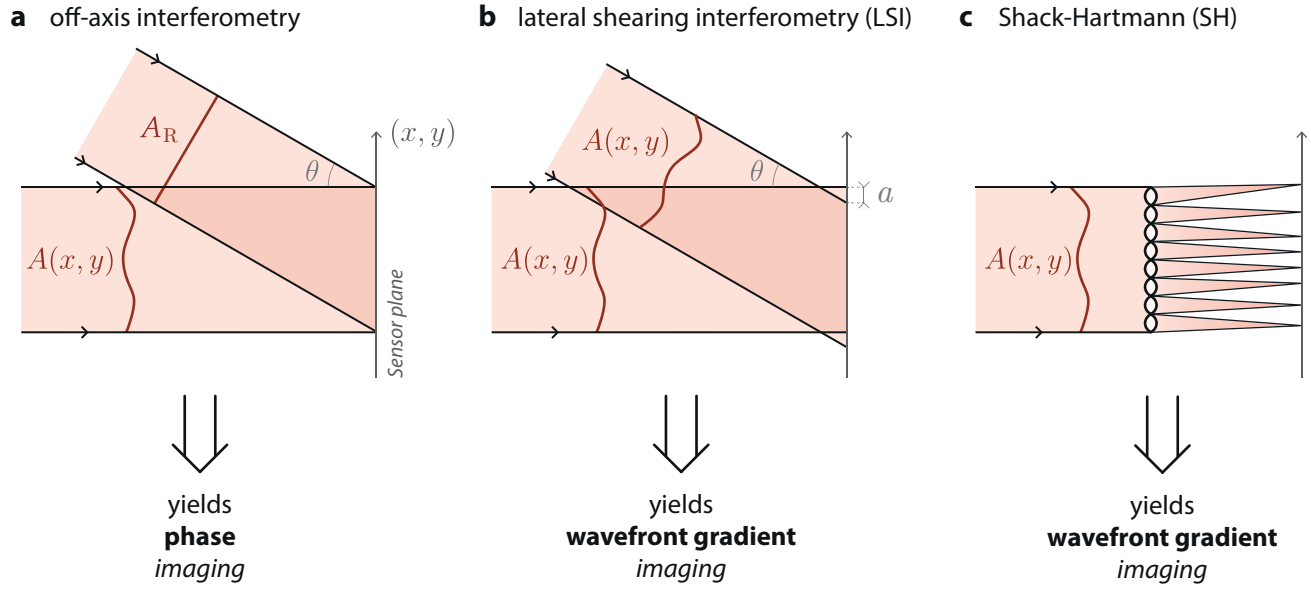

Fig. 2. Three different experimental configurations to access the phase, or equivalently the wavefront, of a light beam. (a) Off-axis interferometry, (b) off-axis lateral shearing interferometry and (c) Shack-Hartmann wavefront sensing.

the sensor plane (Fig. 3c). The four images are shifted by only a fraction of Γ (typically $\Gamma/4$) (Fig. 3a).

Let us adapt Eq. Eq. (4), related to LSI, to the case of QLSI and the use of a grating. For the sake of simplicity, we write the equations with only two diffraction orders instead of 4, say along the x direction. Equation Eq. (4) now reads

$$\begin{aligned} I_c(x,y) =& |\frac{1}{\sqrt{2}}A(x+a,y)+\frac{1}{\sqrt{2}}A(x-a,y)|^2 \\ =& \frac{1}{2}I(x+a,y)+\frac{1}{2}I(x-a,y) \\ &+\sqrt{I(x+a,y)I(x-a,y)}\cos\big[(\mathbf{k}_+-\mathbf{k}_-)\cdot\mathbf{r} \\ &+\varphi(x+a,y)-\varphi(x-a,y)\big] \\ =& i_1(x,y)+i_2(x,y)\cos\big[(\mathbf{k}_+-\mathbf{k}_-)\cdot\mathbf{r} \\ &+\varphi(x+a,y)-\varphi(x-a,y)\big] \end{aligned} \quad \textbf{(5)}$$

where $\mathbf{k}_\pm = [\pm k\sin(\theta),0,k\cos(\theta)]$. The intensity prefactors have been re-written i_1 and i_2 for the sake of clarity. Each of the 4 beams propagates along an angle θ following the Bragg's law: $\lambda = \Gamma\sin\theta$. Let d be the grating-sensor distance, the lateral shift a of each image replica reads $a = d\tan\theta$. Using these two relations, which only exist when using a grating (and not a wedge plate for instance), recalling that $\varphi = 2\pi W/\lambda$, and assuming $\theta \ll 1$, Eq. Eq. (5) can be simplified and now reads:

$$I_c(x,y) = i_1(x,y)+i_2(x,y)\cos\left[\frac{4\pi}{\Gamma}(x+d\nabla_x W(x,y))\right] \quad \textbf{(6)}$$

When considering, not 2, but 4 beams, the final expression is more complex, also involving derivatives along y, $x+y$ and $x-y$,[27] and does not yield fringes but an array of bright spots, as shown in Fig. 3c. Four important comments can be made on this particularly simple expression:

1. The Bragg's law makes the phase φ disappear from the equation, in favor of the wavefront W. Because of the use of a grating, QLSI becomes a *wavefront* imaging technique, and is not a *phase* imaging technique.

2. The wavelength (or the k vector), which was dominant in Eq. Eq. (4) related to LSI, now disappeared in Eq. Eq. (6) related to QLSI. The wavelength does not affect the measurements and does not need to be known to reconstruct the wavefront gradient. It is a benefit of using a grating, compared with a wedge plate for instance. As a consequence, QLSI is an achromatic technique and can be used with a broad band illumination, e.g., from light-emitting diode or lamps. It is even recommended to avoid laser illumination, which gives rise to unwanted fringes like in DHM. However, the $0-\pi$ checkerboard phase pattern of a QLSI cross-grating is created by etching the glass substrate. Thus, the cross-grating is supposed to work optimally for a particular wavelength. However, a deviation from the $0-\pi$ values only reduces the signal-to-noise ratio; it does not yield biased measurements. In practice, a single QLSI grating can be working properly over a range that typically spans from 500 to 800 nm, i.e., covering the full visible range. The periodicity of the fringes only depends on the grating period Γ, and it precisely equals $\Gamma/2$ (all the holes of the grating, being 0 or π, create identical bright spots on the camera plane, which doubles the spatial frequency of the grating). Thus, the fringes periodicity does not depend on anything else and cannot be changed, for instance by changing the wavelength or any tilt angle of optical components.

3. Periodic fringes are observed for any grating-sensor distance d, and with the exact same carrier-wave periodicity. The light wave propagating after the grating is thus propagation-invariant, just like a Bessel beam. A shadow-like light propagation occurs[12, 26] (Fig. 3d). This singular and counterintuitive wave propagation after a QLSI grating is similar to the pattern observed after a Fresnel biprism where, also, two waves propagate along two opposite angles $\pm\theta$, overlap, and interfere. This propagation-invariance created by a QLSI grating comes from the $0-\pi$ checkerboard phase pattern and is what makes the QLSI grating so convenient, and is the basis of the patent from Primot et al.

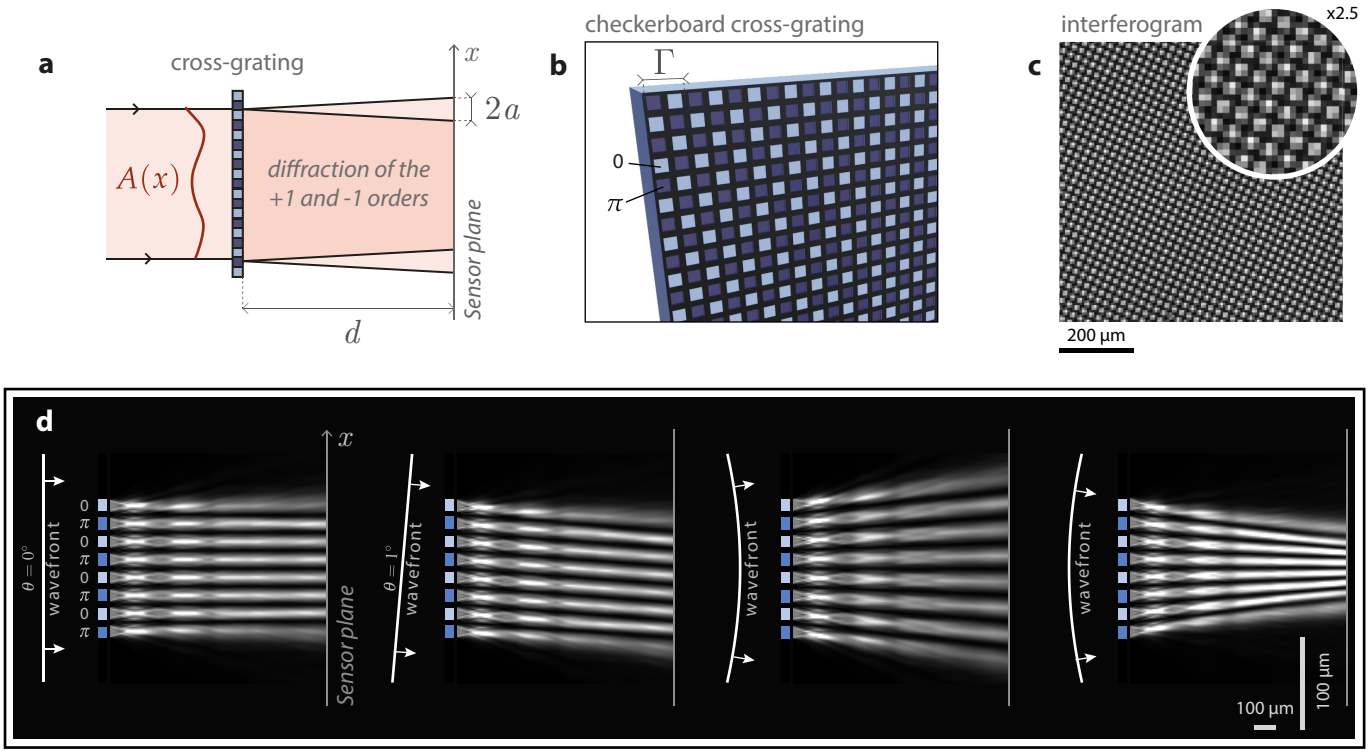

Fig. 3. QLSI principle. (a) Side view of a wavefront diffraction between a QLSI cross-grating and the camera sensor, featuring 2 image replicas along two directions (two other replicas exist along y but are not represented here). (b) Schematic of a QLSI cross-grating. (c) Typical raw intensity image recorded by the camera, which consists or a periodic array of bright dots with a period of $\Gamma/2$. (d) Numerical simulations of the propagation of light between the grating and the camera sensor, for different wavefront profiles, namely uniform, tilted, concave and convex. Reprinted with permission for [26]. Copyright 2021 IOP Publishing.

from 2000.[12, 28] Without the $0-\pi$ checkerboard, the light pattern would become rapidly blurry after a few tens of micrometers of light propagation. A contrasted pattern would be recovered only periodically at wavelength-dependent distances, according to the Talbot effect. As a consequence, with a QLSI grating, the Talbot effect is cancelled and the grating-sensor distance d is no longer critical. It can be continuously adjusted to any value. The further, the better the sensitivity. However, d has to remain within a reasonable range to avoid artifacts and loss of resolution.[29]

In practice, upon wavefront distortion, the bright-spot pattern gets distorted, displaced, and the displacements of the dots (barely visible to the naked eye) follow a simple shadow description as in ray-optics (Fig. 3d). Note that this is exactly how SH wavefront sensing works. Interestingly, although the two families of wavefront imaging techniques depicted in the previous section looked completely different (LSI and SH wavefront sensing, Fig. 2b vs Fig. 2c), QLSI can be understood in either ways.[14, 30] QLSI bridges the gap between these two very different wavefront imaging approaches. Although the name of the technique, QLSI, favors an LSI description, the SH description is equally valid and even easier to understand and explain to a non-specialized audience.

While the QLSI pattern of the cross-grating remains the most popular option, variations of this cross-grating have been used, with 3-fold or 4-fold symmetries [31], with different designs of the unit cell [32–35] or a binary random mask [36]. A recent study even demonstrated the possibility to use a non-periodic optical element, simply consisting of a thin diffuser [22], which creates a speckle-like pattern on the camera. This modality slightly reduces the spatial resolution and/or the field of view compared with QLSI, but remains much better than Shack-Hartmann, and cost-effective. This technique recently proved effective for applications in 3D-nanolocalization of nanoparticles[37] and chemistry at the microscale.[38]

3. QLSI FOR MICROSCOPY: CROSS-GRATING WAVEFRONT MICROSCOPY (CGM)

A. Basic principle

When implemented on a microscope, a QLSI camera measures wavefront distortion created by microscale, transparent objects lying on the object plane (Fig. 4a). If $n(x,y,z)$ is the refractive index distribution of this object, then the wavefront distortion equals the optical path difference (OPD) $\delta\ell = W$ defined by

$$\delta\ell(x,y) = \int (n(x,y,z) - n_0)\mathrm{d}z \qquad (7)$$

where n_0 is the refractive index of the surrounding medium (Fig. 4b). In the case n is uniform, Eq. Eq. (7) becomes

$$\delta\ell(x,y) = (n - n_0)h(x,y). \qquad (8)$$

where h the thickness profile of the object. These expressions are valid in the projective approximation, where ray-optics applies and where optical rays are not markedly deviated by refraction. For objects with dimensions close to the wavelength of the incoming light, diffraction takes the lead and diffraction rings

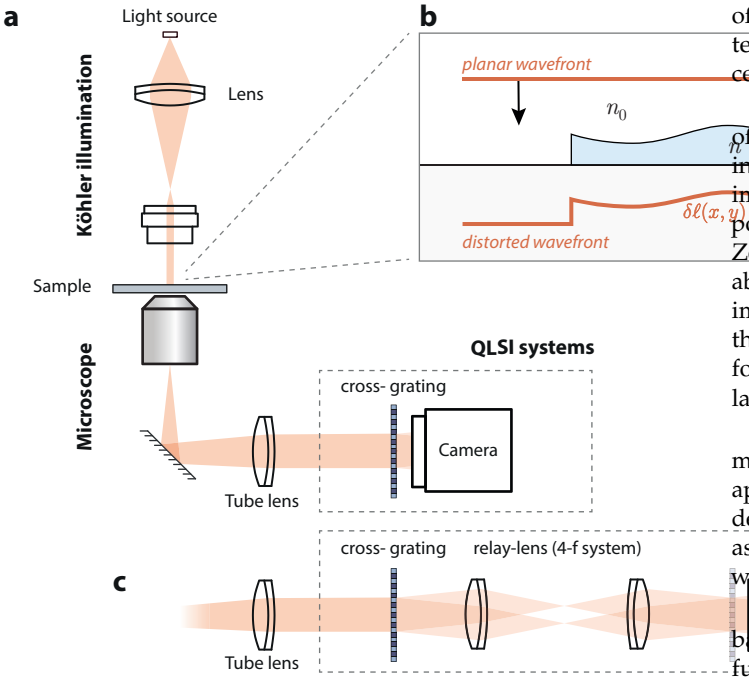

Fig. 4. Schematic of a CGM setup based on QLSI. (a) Experimental setup, coupling a microscope with a QLSI cross-grating and a camera. (b) Focus on the object plane of the microscope where an incident planar wavefront is distorted by the imaged object. (c) Derived implementation of QLSI where the cross-grating is re-imaged in front of the camera by a relay-lens system.

can be observed, and this simple description is no longer valid. However, images can still be acquired, even if they exhibit Airy-like patterns, and quantitative information can still be extracted (see Sect. B related to nanophotonics applications).

B. Reference acquisition

In practice, the wavefront of the microscope illumination is never perfectly flat. Imperfections, aberrations, pieces of dust on the optics, etc, makes the acquisition of a reference image necessary in CGM, which is subtracted during the image processing. Thus, each image processing algorithm requires the specification of a reference interferogram in addition to the interferogram of interest.

Ideally, the reference image is acquired over a blank area of the sample. For applications in biology, where cells are cultured in high confluence, it is not always possible to find a clear area. One way to circumvent this limitation consists in manually moving the sample stage, quite rapidly, during the acquisition of typically 30 images that are subsequently averaged to create the reference interferogram. The moving-trick is effective if the exposure time per frame is at least 80 ms, in order to benefit from a blurring effect on each image.

C. Background correction

For long acquisitions, some low-spatial-frequency distortions in the OPD image may appear over time (typically minutes to hours). They can be easily suppressed. Different algorithms have been developed for this purpose. One can simply apply a high-pass filter to the image, but this method has to be used with caution. It enables the clear visualization of the interior of living cells, but the quantitative nature of the measurements tends to be lost, especially with large cells, such as eukaryotic cells [39].

Another approach that does not affect the quantitativeness of the measurements is to segment the cells, and fit the remaining background area with polynomials to define a background image to be subtracted. Reference [40] reports good results with polynomials up to the 8th order. Some studies report the use of Zernike polynomials.[41, 42] They are relevant to quantify the aberrations on circular images, but fails in correcting rectangular images, especially on the image corners. We rather recommend the use of Legendre polynomials when imaging biological cells for instance, which constitute a orthonormal basis for rectangular images.

The group of Kirschner introduced a background correction method illustrated by CGM measurements, although it could be applied to any QPM [43]. It looks more efficient than the method described in Ref. [40]. In particular, the authors used tricks such as using medians instead of means, and mixing wavefront with wavefront gradient images for a better segmentation.

Pradeep et al employed a rolling-ball algorithm to flatten the background, simply using the MATLAB `imtophat` and `strel` functions.[44] The procedure eased the segmentation of living neurons and their neurites.

Background distortion may affect dry mass measurements, but mainly for large cells. For micrometric objects, such as bacteria or neurites, dry masses can be computed accurately, even without background correction, by considering as a reference OPD value the outer boundary of the cell.[45]

D. Wavefront sensing vs wavefront microscopy

Wavefront *sensing* is a common name, usually associated with Shack-Hartman, and that normally refers to measurements of beam aberrations, by extracting moments of first Zernike polynomials.[17–19] Although QLSI is sometimes referred to as a wavefront *sensing* technique, QLSI does much more than simply sensing aberrations, thanks to its high-definition: it does *imaging*. Thus, describing QLSI or CGM as wavefront *sensing* looks reductive, and the names wavefront *imaging* and wavefront *microscopy* should be favored.

E. Phase vs wavefront

Although CGM is a wavefront microscopy technique, it has always been assimilated as a phase imaging technique since its introduction in 2009. The aim of this imprecision was to better disseminate the technique within the biology community, more familiar with phase microscopy, and for which wavefront sensing looks reductive. The aim was also to make better understand that CGM occupied the same playground as QPMs. Indeed, phase and wavefront are proportional quantities (Eq. Eq. (1)), and both of them can yield dry mass measurements, for instance. However, this intertwining vision gives rise to confusion. Often, QLSI articles speak extensively about "phase" while no phase measurements are reported. Some articles even report "phase" images in nanometer units, mixing phase and OPD. In most QLSI-related studies, it would suffice to simply and exclusively speak about wavefront or OPD. This singularity (measuring a wavefront profile) can be seen as a strength of CGM. It should not be eluded.

4. HISTORICAL REVIEW OF THE APPLICATIONS

Albeit invented in the early 2000,[12, 28] when QPMs were starting to develop, no applications of QLSI was envisioned in microscopy at that time. The field has been progressing mainly with the works of the groups of Primot and Chanteloup, and supported by the creation of a French company, Phasics S.A. in 2003, exploiting the patent of Primot *et al.* At that time, QLSI was rather aimed at challenging SH wavefront sensing applications in adaptive optics or optical metrology.

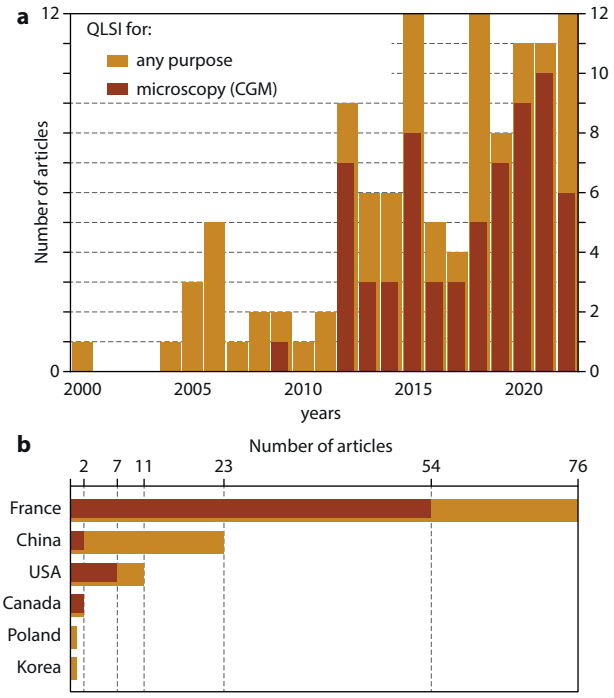

Fig. 5. Statistics on the 114 articles reporting QLSI experiments, both for general purposes, and for microscopy (CGM). (a) Number of peer-reviewed articles published over the years, since the invention of the QLSI grating in 2000, until September 2022. (b) Number or peer-reviewed articles published in each active country.

Fig. 5a shows statistics on the peer-reviewed publications related to QLSI, implemented or not on a microscope. The first use of a QLSI device in microscopy was reported in 2009, through a collaboration between the group of Monneret and the Phasics company.[27] In a pioneer article, the authors reported the use of QLSI for imaging living cells, and demonstrated the capability of wavefront microscopy to tackle applications in biomicroscopy previously reserved to QPM techniques such as DHM. The relevance of the use of QLSI in microscopy, i.e., cross-grating wavefront microscopy (CGM), arises from three features: the high-definition of QLSI (compared with SH), its simplicity, and its low sensitivity to environmental perturbations.

Since then, more and more research groups have been using CGM systems on microscopes, for long in France, and more recently in other countries. Today, around 15 groups in the world (8 in France, 5 in the USA, 1 in China and 1 in Canada) are actively using CGM (Fig. 5b), and we expect this number to rise in the coming years.

The objects of interest that have been observed over the field of view of a microscope since 2009 are depicted in Fig. 6. They consist of (i) biological cells, the first and more important application of CGM, (ii) microscopic temperature gradients, where CGM turns into a temperature microscopy technique, (iii) nanoparticles, (iv) 2D materials, such as graphene, (v) metasurfaces, and (vi) microscale surface topography, in particular to characterize optical damages made by pulsed lasers on optical components.

Most of these studies can be described as belonging to two main fields of applications: biology and nanophotonics. The two next sections describe these two fields of application, while a third one describes less-developed application related to surface topography.

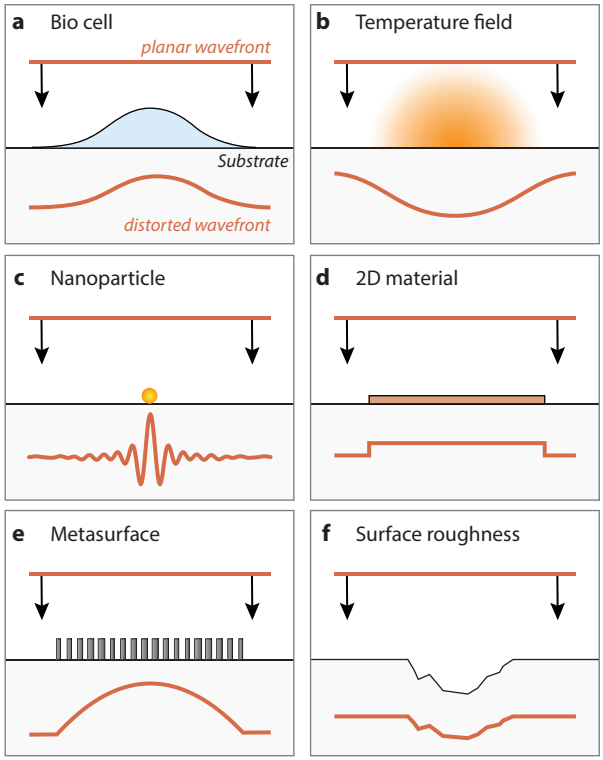

Fig. 6. Different objects of interest in cross-grating wavefront microscopy. (a) A biological cell, (b) a microscale temperature field, created by a laser heating or resistive heating of a microwire, (c) a nanoparticle, (d) a piece of 2D material, such as graphene, (e) a metasurface and (f) a laser damage on a surface.

A. Applications in cell biology

As mentioned above, the first use of a QLSI camera on a microscope (an approach referred to as CGM here) was reported by Bon *et al.* in 2009, in collaboration with the Phasics company.[27] In this work, the authors demonstrated that wavefront imaging could map the optical path difference (OPD) of a biological sample with a spatial resolution and sensitivity that challenged the existing quantitative phase microscopy (QPM) techniques. CGM has been investigated by this same group for a decade, followed by some others very recently.

Unlike fluorescence microscopy approaches, QPM techniques, and in particular CGM, are label-free and non-invasive.[50] They do not require the modification of the sample, do not suffer from photobleaching and blue light toxicity. For these reasons, they can be used to image biological samples for arbitrarily long periods of time. QPMs do not offer the specificity

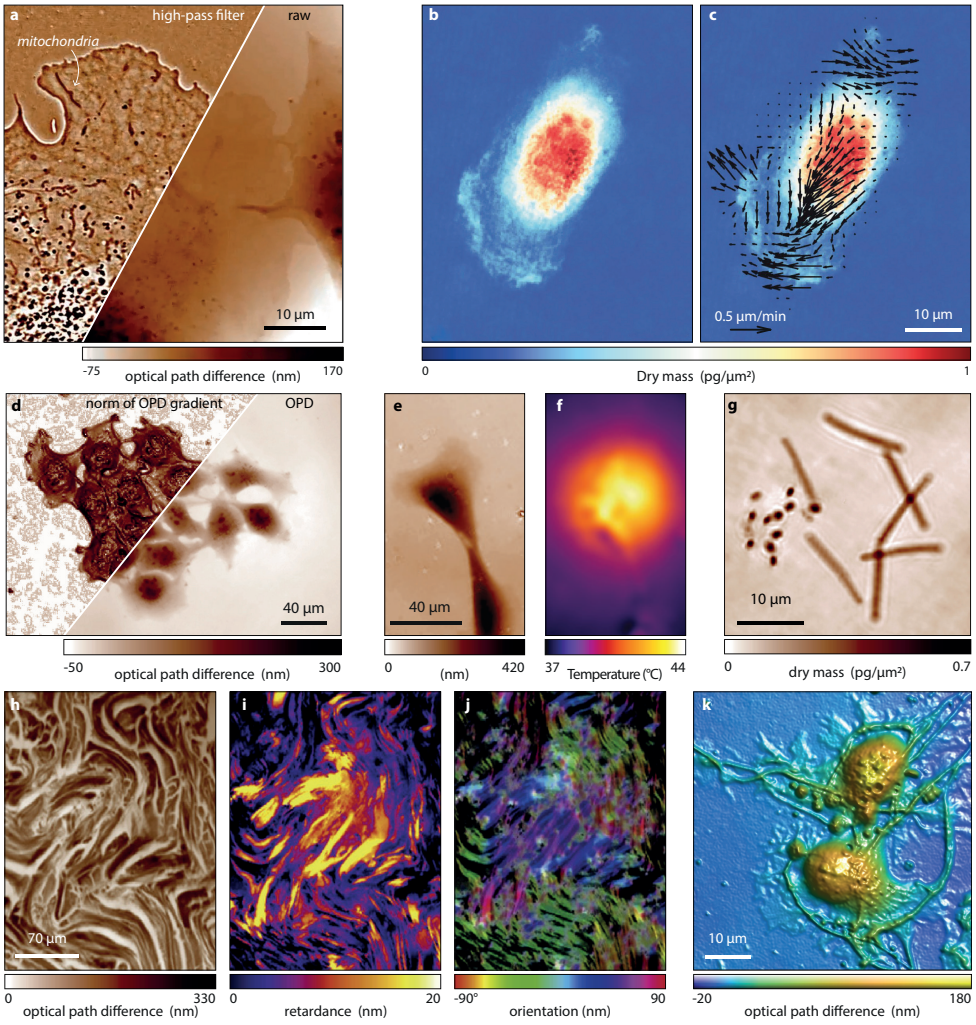

Fig. 7. Overview of CGM images related to applications in biology. (a) OPD image of a living CHO cell (180×, 1.49 NA, home-made CGM system). Reprinted with permission from [39]. Copyright 2014 Biophysical Society. (b,c) Dry mass images of a living RPE cell (120×, 1.3NA, Sid4Bio/Phasics). The measured mass velocity field overlays the image in (c). Adapted with permission from [46]. Copyright 2022 Springer Nature https://creativecommons.org/licenses/by/4.0/. (d) OPD image of living COS-7 cells, along with the image of the norm of the OPD gradient, as a means to better visualize the cells boundaries and ease segmentation (40×, 1.3NA, Sid4Bio/Phasics). Reprint with permission from [40]. Copyright 2015 SPIE. (e) OPD image of RPE cells. (f) Temperature map of the same cells as (e) upon laser heating measured in parallel by CGM. Reprint with permission from [47]. Copyright 2018 Wiley. (g) Dry mass image of Geobacillus Stearothermophilus bacteria under germination activated by laser heating of gold nanoparticles (66×, 1.3NA, home-made CGM system). Adapted with permission from [48]. Copyright 2022 Nature Springer https://creativecommons.org/licenses/by/4.0/ (h) OPD of a human breast slice tissue (40×, 0.75NA, Sid4Bio/Phasics); (i) Retardance image associated with (h); (j) Image of the orientation of the ordinary axis associated with (h); Reprinted with permission from [49]. Copyright 2018 Elsevier. (k) OPD image of hippocampal neural cells,[29] (40×, 1.35NA, SID4-sC8/Phasics).

of fluorescence imaging, but appear as a powerful alternative, and in particular to get a valuable information that fluorescence cannot access: the dry mass of living organisms, as explained further on.

Here is below a review of the different imaging modalities of CGM that have been developed in the context of applications in biology.

Label-free imaging of organelles. After its introduction in 2009, Bon *et al.* highlighted the ability of CGM to image living cells with a sufficient resolution to observe vesicles,[51] mitochondria, and even microtubules[39] (Fig. 7a), although all these organelles usually need to be fluorescently labelled to be imaged. An impressive movie showing chains of mitochondria moving along microtubules is provided with Ref. [39] . In this article, the authors give many hints to optimise the spatial resolution in CGM.

Dry mass. The refractive index of an object being directly dependent on its mass density, QPM images contain information that can be used to retrieve the dry mass of imaged cells. Here lies one of the most important interest of QPM techniques: the ability to measure masses using light. The method simply consists in summing the pixels of the OPD image of the object of interest:

$$\delta m = \gamma^{-1} \iint W(x,y)\mathrm{d}x\mathrm{d}y = \gamma^{-1} p^2 \sum_{\text{pixels}} W_{ij} \qquad (9)$$

where δm is the dry mass of the imaged object and γ is the refractive index increment (the inverse of the dry-mass density). Although this idea has been introduced in 1952,[52] one had to wait the development of effective QPM techniques to see its demonstration with high-resolution and precision, in 2008 and in 2009, by Popescu et al.[9] and Rappaz et al.[10] Since then, dry mass measurements using QPM have been reported by many groups for a large variety of cell types (mammalian, cancerous, bacteria, yeast, neurons, etc).[53]

The OPD can be converted in a straightforward manner into dry mass surface density using

$$\delta\rho = \gamma^{-1}\delta\ell, \quad (10)$$

$$\delta\rho\ [\mathrm{pg}/\mu\mathrm{m}^2] = 5.6\times10^{-3}\delta\ell\ [\mathrm{nm}]. \quad (11)$$

Interestingly, neither the knowledge of the wavelength nor of the pixel size are required to convert an OPD image into a dry mass surface density. For instance, 100 nm of OPD always means a dry mass surface density of 0.56 pg/μm^2, no matter the camera and the microscope. For this reason, wavefront imaging looks more natural to retrieve dry mass than phase imaging, which requires to knowledge of the wavelength as well. This benefit of wavefront microscopy is only conceptual, not practical, because the wavelength in the experiment is always known anyway.

Cells in culture are highly dynamic, featuring strong variations of shapes and volumes, within time scales ranging from sub-second for small vesicles to several days. The high contrast of OPD images using CGM and the quantitative nature of the dry mass measurements enable the effective monitoring of this cell dynamics. In particular, observations can be conducted for arbitrarily long periods of time, tenuous objects such as lamellipodium, mitochondria or microtubules of the cell can be clearly observed, and dry mass measurements quantify the growth rate. Following these benefits, several articles have been published for almost a decade that we present hereinafter.

The first use of CGM to measure dry masses dates from 2015,[40, 54] where the authors provided a detailed study of the accuracy of the measurements, and how it depends on the segmentation of the cell, the coherence of the illumination, and the focus. A particular attention was put on the segmentation algorithm. The segmentation procedure involves the use of the two OPD gradients along x and y, which are the two images that are primarily obtained from the raw camera image. Fig. 7d plots the norm of the OPD gradient that is used in the segmentation algorithm. This way of visualizing OPD images helps the segmentation, but it looks also very interesting as a means to improve the image contrast, although it was not noticed in the article. Moreover, since this image does not require image integration, it can be computed much faster than the OPD, which is of interest for fast live imaging.

In 2015, Ohene *et al.* benefited from this high contrast of CGM to monitor the deformation and condensation of living cells during apoptosis.[55] The study mainly benefited from the good contrast of CGM, not from the quantitative nature of the measurements.

In 2015, the group of Piel used CGM to monitor the dry mass of cells during mitosis, along with their volume measured using fluorescence.[56] The authors showed that the dry mass did not vary while the volume increased, evidencing a decrease in mass density during mitosis. This work illustrates the benefit of coupling CGM with fluorescence microscopy, a union that is facilitated by the fact that CGM can be easily implemented on standard microscopes.

In 2019, Pognonec *et al.* stressed the ability of CGM to replace fluorescence microscopy in some studies, and suppress its inherent invasiveness.[54] The authors have shown that CGM can replace fluorescence-activated cell-sorting (FACS) that normally requires non-physiological cell handling or cell labelling.

In 2020, Llinares *et al.* used CGM to monitor the transmembrane water fluxes following hyper/hypertonic stresses.[57] The readout was only the OPD profile. No measure of the cell surface or dry mass were performed. The issue with this study is that the measured OPD combines n, n_0 and h according to Eq. Eq. (8), and these three parameters varied during the experiments. However, the authors considered that only the refractive of the cell n was varying. Neither CGM nor any QPM can easily measure water content variations within live cells, because the measured OPD signal is mainly stemming from the dry mass content of the cell. For instance, as mentioned above, to monitor any cell volume variation at constant dry mass, the group of Piel had to combine CGM with fluorescence measurements.[56] They could not have shown anything with only OPD measurements.

In 2021, the group of Zangle conducted dry mass measurements using CGM on neural cells.[44] The group could automatically segment somas and neurites, and measure their cumulated dry mass over the field of view of the microscope for 120 h. First, this work demonstrates the ability of CGM to conduct experiments for arbitrarily long periods of time without affecting the cells (in particular cells as sensitive as neurons), a strong benefit compared with fluorescence microscopy. Second, the authors could provide quantitative data on how mass is distributed throughout the cellular bodies and neurites during their growth. Third, many QPM techniques can hardly measure the dry mass of biological objects as tenuous as neurites, highlighting the high sensitivity of CGM.

In 2021, the group of Reed used CGM and dry mass measurements to rapidly identify lymphoma cells that are resistant to a therapeutic agent and cells that are not, overcoming the difficulty of identifying drug-tolerant sub-populations during the early stage of the treatment.[58]

Machine learning is currently having a strong impact on many fields of research, and QPM is no exception.[59] To feed a machine learning algorithm, many quantitative features can be extracted from an OPD image. The dry mass and dry mass density, as already mentioned, but also the area, the optical volume, the eccentricity, the perimeter, the shape factor, among others.[60] In 2021, the group of Teitell used many of such parameters extracted from CGM images to feed a machine learning algorithm and train it to classify tumor-reactive T cells, in a rapid and label-free manner.[61]

In 2021, the same group contributed to the study of cardiomyocytes (cells in the heart that make it contract) *in vitro* using CGM. They imaged the evolution of the dry mass distribution over 12 h, to investigate migratory characteristics of two cellular populations, which exhibited strong differences.[62]

In 2022, the group of Zangle pushed forward the idea of following mass migration within cells using CGM.[46] By processing successive images of dry mass density, the authors could retrieve the velocity field of mass transport within cells (Fig. 7b,c). The algorithm is based on registration of sub-images of the field of view. This imaging modality provides a valuable and versatile tool for the study of cells in culture because cells are never immobile and because it enables the study of mass transport in addition with mass distribution. The authors called

this technique QPV for quantitative phase velocimetry.

Retardance. Some biological samples are birefringent, meaning that the refractive index experienced by a light beam crossing the sample depends on its polarization. One can define the so-called ordinary (o) and extraordinary (e) axes for which the refractive indices of the materials, n_o and n_e, are different. Using linearly polarized light along the o and e axes leads respectively to the measurements of the following OPD images

$$\delta\ell_o = (n_o - n_0)h, \quad (12)$$

$$\delta\ell_e = (n_e - n_0)h. \quad (13)$$

For an arbitrary polarisation angle θ, the measured OPD reads [63]

$$\delta\ell(\theta) = \frac{\delta\ell_o + \delta\ell_e}{2} + \frac{\delta\ell_o - \delta\ell_e}{2}\cos 2(\theta - \theta_0) \quad (14)$$

where θ_0 is the orientation of the o axis. Using this expression, acquiring a series of OPD images at various θ angles enables thus the retrieval of the retardance of the sample, defined by

$$\Delta = \delta\ell_o - \delta\ell_e. \quad (15)$$

Aknoun *et al.* introduced this methodology in 2015 to map the retardance of birefringent biological samples,[40] and later in 2018 for the study of the extracellular matrix of biopsies[49] (Fig. 7h-j).

Live cell temperature. Temperature variations, especially in a liquid, produce variations of the refractive index. Refractive indices of liquids tend to decrease with temperature due to the expansion of the liquid. As a consequence, any temperature gradient within a fluid has the ability to affect a light beam, a phenomenon sometimes called a thermal lens effect (Fig. 6b) [64–66]. In 2012, we introduced the possibility to map the wavefront distortion created by the laser heating of plasmonic nanoparticles, using CGM, and retrieve the temperature profile from this measurement.[67] This work opened an unexpected functionality of CGM: its use as a temperature microscopy technique. Normally, imaging temperature at the microscale required the use of fluorescent compounds with temperature-dependent properties [68]. Temperature microscopy using CGM provided at least three benefits compared with fluorescence-based approaches: (i) it is label-free and non-invasive, (ii) it does not suffer from common artefacts related to fluorescence microscopy [69–72] and (iii) it does not suffer from photo- and thermo-bleaching and can investigate arbitrarily large temperature increases,[73] while common fluorescent molecules bleach at around 60°C.

This approach has been used to map the temperature distribution within and nearby living cells created by microscale laser heating of gold nanoparticles (Fig. 7e,f), to guide the migration of cells [74] and to study the expression of heat-shock proteins, at the single-cell level [47]. More recently, it was used to measure the temperature distribution at the microscale upon laser heating of thermophilic bacteria and archaea, avoiding the use of a common heating stage with limited temperature range and large thermal inertia [48]. Figure 7g displays an OPD image of the germination of *Geobacillus stearothermophilus* induced by laser heating, in which CGM was used both for temperature measurements and dry mass measurements. Note that DHM also recently demonstrated its ability to map microscale temperature distributions.[75, 76]

B. Applications in Nanophotonics

Due to its high resolution and sensitivity, CGM managed to challenge applications in bioimaging that were normally dedicated to QPM techniques, but it also opened a domain of investigation: the one of nanophotonic objects. Imaging nanophotonic objects such as 2D materials or nanoparticles using CGM enables the mapping of the full electromagnetic field of their image through a microscope (in the scalar approximation). This information is sufficiently rich to extract all the optical properties of the imaged nano-object. Hence, CGM appears not only here as a high-contrast microscopy tool, but also as a metrology tool, exactly like in biology where CGM could also quantitatively measure dry masses of living cells.

In the following, we explain how CGM has been used to map temperature around plasmonic nanoparticles under illumination, and optically characterize 2D-materials, nanoparticles, and metasurfaces.

Temperature microscopy. Heating metal nanoparticles using light at their plasmonic resonance relates to a field of research named thermoplasmonics, with applications in biomedicine, fluid dynamics, Sun light harvesting among others [81–83]. Laser-heating of metal nanoparticles is also a means to conduct fundamental research in many fields of science because many fields of science feature temperature-induced effects, e.g., chemistry, biology, fluid dynamics, phase transition, etc. Heating metal nanoparticles, and in particular gold nanoparticles, enables the study of all these fields at the nano and micro scales. The main challenge of this approach is not to heat, but rather to measure the resulting temperature increase.

As explained in the biology part above, CGM can be used as a temperature microscopy technique, by probing and post-processing the wavefront distortion created by thermal-induced refractive-index gradients (Fig. 6b). Before being applied to mapping the temperature in living cells, it was applied to map the temperature around gold nanoparticles heated by laser absorption. From the raw interferogram image, not only the temperature distribution in 3D can be determined [84], but also the 2D heat source density (power per unit area) on the substrate (Fig. 8e-h) [67]. Since 2012, this label-free temperature imaging technique has been used in around 16 articles, mainly by our group. We shall not describe all the work related to this technique here. We just mention the most important developments.

In 2014, thanks to the possibility to image temperature fields at arbitrarily large temperature using CGM, it was demonstrated that water boiling occurs around metal nanoparticles at around 200°C, much above the boiling point of water [73]. This effect is called superheating, and occurs because of the absence of nucleation point (scratches, pieces of dust). This phenomenon led us to demonstrate two applications: (i) the introduction of the concept of hydrothermal chemistry at the microscale [85] and (ii) the possibility to activate thermophilic organisms at arbitrarily high temperature using laser heating of gold nanoparticles [48] (Fig. 7e,f).

When heating arrays of nanoparticles with laser beam, the resulting temperature profile is usually Gaussian-like, which may be detrimental for applications that require a unique, uniform temperature distribution, e.g., in chemistry or biology. To solve this issue, two approaches have been developed, supported by CGM temperature measurements: (i) using non-uniform gold nanoparticles samples [86] or (ii) using non-uniform laser beam profiles heating uniform gold nanoparticles arrays [87, 88]. In these two similar approaches, any temperature profile at the microscale could be produced, e.g., uniform, linear, parabolic, etc. The second approach already led to applications in thermophoresis control at the microscale [89] and in cell biology[48].

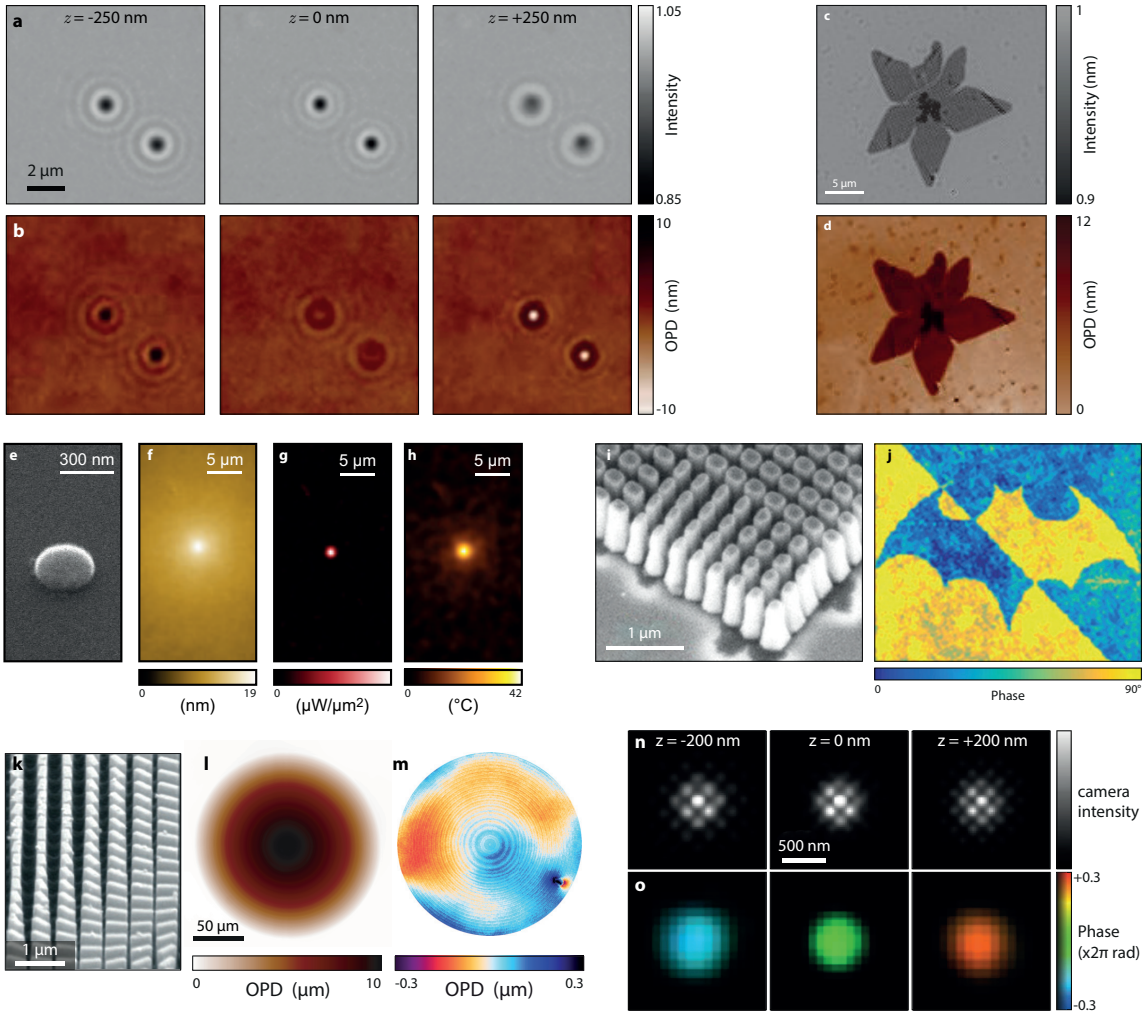

Fig. 8. Overview of CGM images related to applications in nanophotonics. (a) Intensity images of two 100-nm gold nanospheres at different focus values z; (b) Associated OPD images showing a contrast inversion of the OPD when passing the focus. Reprinted with permission from [77]. Copyright 2015 Nature Springer. (c) Intensity image of a molybdenum disulfide (MoS_2) flake and (d) associated OPD image. Reprinted with permission from [78]. Copyright 2017 the American Chemical Society. (e) Scanning electron microscope (SEM) image of a gold nanostructure; (f) Wavefront distortion upon laser heating of the nanoparticle; (g) heat source density processed from the OPD image (f); (h) Temperature map processed from image (g). Reprinted with permission from [67]. Copyright 2012 the American Chemical Society. (i) SEM image of the border of a metasurface and (j) phase image of the whole metasurface. Reprinted with permission from [79]. Copyright 2021 De Gruyter. (k) SEM image of a portion of a metalens and (l) OPD image of the metalens, along with (m) the associated OPD aberrations. Reprinted with permission from [42]. Copyright 2021 the American Chemical Society. (n) Interferogram images of 100-nm fluorescent nanobeads, at various focus values z and (o) resulting phase images, weighted by the intensity images. Reprinted with permission from [80]. Copyright 2018 Nature Springer.

Note that DHM was also used to map temperature in 3 dimensions around laser-heated gold nanoparticles in 2019[75] and 2021.[76]

Metrology of 2D materials. In 2017, Khadir *et al.* used CGM to not only image one-atom-thick materials such as graphene with a good contrast, but also fully characterize their optical properties [78]. More precisely, CGM could quantitatively measure the complex refractive index n of 2D materials or equivalently their complex optical conductivity σ defined by

$$\mathbf{J}_{2D} = \sigma \mathbf{E} \tag{16}$$

where $\mathbf{E}$ is the complex electric field amplitude of the light within the 2D material and $\mathbf{J}_{2D}$ the two dimensional electronic current density within the 2D material. The complex optical conductivity σ characterizes thus the response of the 2D material to light in amplitude and phase, and it is all we need to know to fully characterize the optical response of the 2D material. This important physical quantity can be extracted from the normalized transmittance $\sqrt{T}$ and the optical path difference $\delta\ell$ images using the expression

$$\sigma = \varepsilon_0 c(n_1 + n_2)\left[\frac{1}{\sqrt{T}}\exp\left(i\frac{2\pi}{\lambda}\delta\ell\right) - 1\right]. \tag{17}$$

$\sqrt{T}$ and W being images (matrices), σ is also an image, giving the map of the complex optical conductivity of the imaged 2D material. This spatial mapping of σ is an asset compared with more conventional characterization techniques, such as ellipsometry, that can only measure an average of the optical properties of materials over macroscopic areas. With CGM, one can ob-

serve defects, dislocations, etc, and make sure measurements are performed on clean areas.

Of course, the complex refractive index n is more popular in metrology of 2D-materials compared with σ. However, using n makes sense only for a bulk material, not for a 2D material. For a 2D material, n can be used provided a thickness h is assigned to the material. In the case of graphene for instance, one usually considers the interlayer distance of graphite to be the thickness of graphene, but this remains a convention. A single-atom-thick object does not possess clear boundaries.

Importantly, once a thickness h of the 2D material is defined, the refractive index of the material cannot be simply calculated from the OPD image using Eq. Eq. (8): $\delta\ell = (n - n_0)h$. Due to multiple reflections within the 2D materials, this expression is inaccurate, especially for large values of n. For instance, this expression remains a good approximation for graphene, but not for MoS_2. Moreover, this expression would only give the real part of the refractive index, not the imaginary part stemming from absorption. Provided a thickness h is assigned to the material, the complex refractive index n can also be retrieved from σ, by numerically inverting an equation (Ref. [78] , Eq. (10)). This study focused on two 2D materials: graphene and MoS_2 (Fig. 8c,d), which are respectively 1-atom and 3-atom thick, and reported values of σ and n with a very good agreement with the literature.

Metrology of nanoparticles. In 2020, we introduced the possibility to measure the optical properties of nanoparticles imaged by CGM [90, 91]. When imaging sub-wavelength objects, the interpretation of the wavefront profile as an optical path difference (OPD) does not make much sense. The wavefront image is clearly affected by diffraction and looks like an Airy pattern (Fig. 8a,b). Still, one can extract precious information from the transmittance and wavefront images because, once again, the actual electromagnetic field of the nanoparticle image can be mapped. Following the same spirit as with 2D materials, all the optical properties of the nanoparticles can be retrieved from the CGM images. In place of the optical conductivity for a 2D material (see previous paragraph), the meaningful, equivalent quantity for a nanoparticle is the complex optical polarizability α defined by

$$\mathbf{P} = \alpha \mathbf{E}_0 \tag{18}$$

where $\mathbf{E}_0$ is the complex electric field amplitude of the incoming light at the nanoparticle location and $\mathbf{P}$ the complex amplitude of the dipolar moment of the nanoparticle. α can be determined from the normalized intensity T and OPD $\delta\ell$ images using this expression:

$$\alpha = \frac{i\lambda n}{\pi} \iint \left[1 - \exp\left(i\frac{2\pi}{\lambda}\delta\ell\right)\right] \mathrm{d}x\mathrm{d}y. \tag{19}$$

The way of calculating α is thus similar to σ, but with an important difference: Eq. Eq. (19) involves an integral over the image, i.e., a pixel summation (just like for the dry mass), making α a scalar value, no longer a map of the object. In nanophotonics, α is difficult to measure. One usually rather measures the three cross-sections (extinction, absorption and scattering). Interestingly, the sole knowledge of α enables the determination of the three cross-sections at once, from a single CGM image of the nanoparticle, a task that normally requires three different setups. Here are the expressions to be used:

$$s_{\mathrm{ext}} = \frac{k_0}{n}\mathrm{Im}(\alpha), \tag{20}$$

$$s_{\mathrm{sca}} = \frac{k_0^4}{6\pi}|\alpha|^2, \tag{21}$$

$$s_{\mathrm{abs}} = s_{\mathrm{ext}} - s_{\mathrm{abs}}. \tag{22}$$

The expression giving the extinction cross section s_{ext} is exact no matter the size and shape of the nano-object. However, the two following equations are only valid for dipolar nanoparticles, typically not exceeding 100 nm, although no detailed investigation of the limitation of these expressions has been reported.

At the microscope focus, the OPD image of a metal nanoparticle undergoes an inversion of the contrast (Fig. 8a,b). This feature led Wenger and Bon to the idea of an autofocus system based on the use of metal nanoparticles imaged using CGM [77]. This contrast inversion enables the tracking of the focus of a microscope with a precision of 2.7 nm in the axial direction. The authors patented the method in 2014 [92].

In the same spirit, in 2018, Bon managed to conduct CGM measurements on single fluorescent emitters over a dark background, which is not the standard configuration in CGM [80, 93]. One cannot speak about distortion of wavefront here. The authors of the study rather measure the curvature of the emitted fluorescence light beams, which exhibits an inversion when passing the focus (Fig. 8n,o). Quantifying this curvature enables the accurate determination of the z-position of an emitter. This principle was combined with localization microscopy on actin filaments networks in 3 dimensions. Note that in this article, the QLSI grating was special, in the sense that it only consisted of a $0 - \pi$ checkerboard pattern without opaque lines.

Let us mention that off-axis DHM was also used recently to characterize single nanoparticles,[94–96] with very similar sensitivity and spatial resolution as CGM.

Characterization of metasurfaces. Metasurfaces are non-uniform, dense arrays of nanostructures that are aiming at playing with the shape of an optical wavefront [97]. For instance, one can design ultra-flat lenses (called metalenses) using this approach. Of course, the efficiency of metasurfaces strongly depends on the nanofabrication process and some deviation from the initial design can be observed, leading to aberrations of the metasurface. Using wavefront imaging seems thus a natural approach to characterize metasurfaces.

In 2019, Berto *et al.* pioneered the use of CGM as a tool to characterize the wavefront distortion of metalenses, in the context of the active control of the focal length of metalenses by resistive heating of a fluid at the microscale [41]. In 2020, Khadir *et al.* reported the use of CGM to finely characterize the optical properties of metasurfaces and their imperfections, in particular in terms of moments of Zernike polynomials (Figure 8k,l,m) [42]. In 2021, the group of Genevet used CGM as a characterization tool of metasurfaces in the context of encryption applications (Fig. 8i,j) [79].

Tackling the field of nanophotonics using wavefront microscopy requires the use of a technique that exhibits both high-resolution and high-sensitivity, because the objects of interest can be very small or very thin, leading to tenuous wavefront distortion. It may explain why no other QPM technique has been used in nanophotonics before. With these four applications (temperature, 2D-materials, nanoparticles, metasurfaces), CGM represents a tool of predilection for metrology in nanophotonics.

C. Applications in surface topography

All the applications listed above are usually conducted on glass coverslips. The roughness of a glass coverslip reported in Ref. [39] is 0.7 nm. Such a roughness is measurable using CGM, which corresponds to an OPD standard deviation of 0.37 and 0.13 nm in air and water respectively. This roughness usually appears as a limitation to observe tenuous objects, but local defects of the planar interface of the substrate can also be the feature of interest for some applications. For instance, in a series of three articles [98–101], the group of Gallais used CGM to characterize microscale damage made by high-energy, focused laser pulses on the surface of optical components. Of particular interest of this series of articles is the use of CGM in a pump-probe, stroboscopic approach to perform time-resolved OPD imaging at the picosecond time scale [99]. The same group also drilled microcraters on glass samples, filled with a liquid of interest, as a means to measure the temperature-dependence of the refractive index of the liquid [102].

5. CGM COMPARED WITH QPM TECHNIQUES

In this part, we compare CGM with QPM techniques, namely DHM, DPM and SLIM, which are among the most popular QPMs, and for which there exists data to be compared with. The experimental setups related to these three QPMs are represented in Fig. 9, where the CGM setup is also recalled.

A. CGM versus DHM

A CGM setup (Fig. 9a) consists of a standard microscope associated with a camera, in which a cross-grating has been added at around 1 mm from the camera sensor [12, 26, 27]. The technique is thus particularly simple to implement. Neither the illumination nor the detection parts of a microscope need to be modified. CGM can be improvised on any scientific microscope, provided it is endowed with a Köhler illumination. In particular, CGM can be easily implemented on a fluorescence microscope.

In DHM (Fig. 10b), a laser illumination needs to be implemented and the laser beam needs to be split before the sample and recombined in front of the camera using beam splitters (Fig. 9b) [103, 104]. DHM requires thus the use of a dedicated microscope.

In 2018, Bélanger *et al.* compared three QPM techniques: transport of intensity equation (TIE), CGM and DHM (Fig. 10c-h) on optical waveguides [105], a study closely followed by another one from Allier et al. also comparing CGM and DHM [106], but on biological samples. As a general conclusion of these articles, CGM and DHM approaches demonstrated similar performances. The main difference is that phase images obtained with DHM display an inherent higher noise level (Fig. 10g), in contrast to CGM images that are naturally smoother (Fig. 10d) because based on incoherent illumination while DHM uses a laser illumination. However, after treatment of the DHM images, both techniques yielded similar image quality (Fig. 10e,h). DHM even featured a slightly better spatial resolution compared with CGM. However, the authors used a Sid4Bio camera (Phasics S. A.), which implies a camera pixel size of $p = 7.4$ µm and a grating pitch of $\Gamma = 59.2$ µm (i.e. a zeta-factor $\zeta = \Gamma/2p = 4$). More recent CGM cameras with $\zeta = 3$ and a $\Gamma = 39$ µm yield higher spatial resolution (Fig. 7k) [29]. In theory, because CGM and DHM image processing methods are both based on a filtering of spatial frequencies in the Fourier space, they both reduce the image definition in the exact same way. It does not mean that the spatial resolution gets affected. If the magnification of the microscope is such that the image of oversampled, the final OPD or phase images of CGM and DHM can reach the diffraction limit.

Also, CGM is achromatic and can be used with broadband illumination and with monochromators, which makes it easy to scan the wavelength and investigate the optical properties of the sample as a function of the wavelength, which is not the case of DHM.[78]

DHM requires the use of a laser illumination, which is likely to produce fringes or speckle on the images (Fig. 10h). On the contrary, CGM can use an incoherent illumination, so that fringes or speckle are never observed. However, the coherent nature of the illumination of DHM, along with the associated zero-NA illumination enables numerical refocusing over large distances using DHM.[2, 76]

In DHM, the use of a reference arm makes the system very sensitive to external perturbations, like air flow, thermal drift or mechanical vibration. This drawback usually creates non-uniform background on the phase images that need to be corrected. This issue is cancelled by common-path techniques, such as CGM, DPM or SLIM.

Like any wavefront imaging technique, which primarily measures a wavefront gradient, CGM is not sensitive to overall variations of the phase of the imaged beam, called a piston. It may be a limitation for some applications, but in general, when imaging microscale scale objects contained within the field of view of a microscope, like cells, the piston is not a quantity of interest.

On the other hand, DHM is capable of measuring phase piston variations over time. DHM also offers the possibility to play with the reference beam independently, for instance by implementing acousto-optic modulators and achieve heterodyne imaging to boost the signal.[107] DHM is also able to reconstruct phase vortices, which was not possible using CGM until recently.[108]

As mentioned earlier, DHM was also used in nanophotonics, recently, to characterize single nanoparticles,[94–96] with very similar sensitivity and spatial resolution as CGM.

B. CGM versus DPM and SLIM

Introduced in 2006 by Park et al.[5, 6], DPM looks similar to CGM in the sense it involves a grating (Fig. 9c). However, there are substantial differences. First, it involves a 1D grating, not 2D. Then, in DPM, the grating is conjugated with the camera (not displaced by a millimetric distance), and there is a relay-lens that makes accessible the Fourier plane where a mask is placed to select and make interfere the 0 order and a 1st order. The particularity of the 0 order is that it is spatially filtered: the hole of the mask is small enough, typically from 10 µm[6] to 150 µm,[109] to fully smooth the corresponding image in the sensor plane. This way, DPM is an off-axis technique, just like DHM, where the reference beam is the zero order. DPM is thus a phase microscopy technique, not a wavefront microscopy technique, although it looks similar to CGM. The benefit of DPM compared with DHM is that DPM is a common-path technique, just like CGM, which makes it less sensitive to external perturbations. The typical noise of DPM images is around 3 nm,[6] 10 times more than CGM (0.3 nm).

Introduced in 2010, SLIM is a QPM that updates a Zernike phase contrast microscope to make it quantitative (Fig. 9d).[7, 110] The basic principle is based on the use of a spatial light modulator (SLM) conjugated with the back focal plane of the objective, that imprints phase rings profiles. By acquiring a series

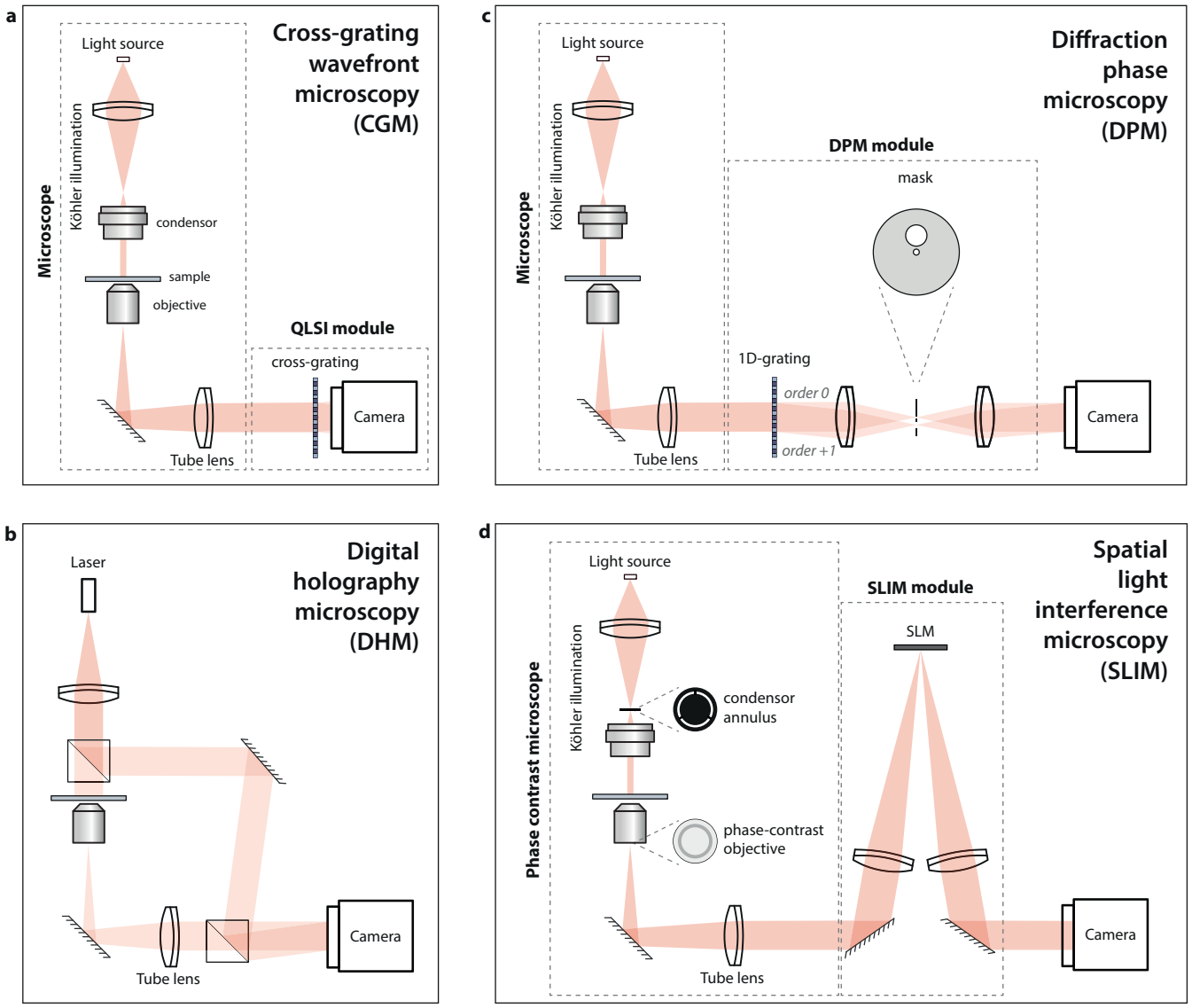

Fig. 9. Schematic of a CGM and QPM experimental setups (a) Cross-grating wavefront microscopy (CGM) in its implementation without a relay lens. (b) Off-axis digital holography microscopy (DHM). (c) Diffraction phase microscopy (DPM). (d) Spatial light interference microscopy (SLIM).

.

of 4 images corresponding to 4 different phase shifts (0, $\pi/2$, π, $3\pi/2$), a quantitative phase image of the sample can be obtained. SLIM was shown to feature a noise amplitude of 0.3 nm on the OPD,[7] similar as CGM.[29].[7] The use of an SLM in SLIM not only makes the system significantly more complex but also polarization dependent. This makes the method incompatible with birefringence measurements and SLIM measurements may be subject to polarization artifacts.

No comparative studies exist between CGM and SLIM or DPM. However, comparison can be made by bringing together images from different articles featuring the same kind of samples. In this spirit, Fig. 11 collects QPM images of neurons that have been acquired using these three techniques, namely CGM, DPM and SLIM, and using similar color-scales. Neurons are composed of a cell body, called the soma, surrounded by neurites, much thinner, that eventually turn into axons or dendrites.

Images of CGM and DPM shown respectively in Figs. 11a and 11b look very similar, at least qualitatively. Since these measurements are made on different neurons, the comparison should remain qualitative. In particular, they are characterized by a bumpy soma. However, Fig. 11c that shows a DPM image from another article does not feature such a bumpy soma. Most of the inner part of the neuron has even a similar OPD value as the surroundings, as if the soma did not contain biological material (dry mass).

The same observation can be made regarding the OPD image of a neuron acquired using SLIM (Fig. 11d). Here again, the soma looks quite empty. Even the neurite in the bottom-right quadrant looks optically thicker than the soma. One can also see a dark area surrounding the soma. These unexpected features observed in Figs. 11c,d typically arise when a high pass filter is applied to the image. For instance, in Ref. [39], Bon et al. applied a high-pass filter on CGM images as a means to better highlight the interior of living cells, and the rendering was very similar to the ones observed in Figs. 11c,d. However, when such a high-pass filter is applied, one naturally loses the quantitative

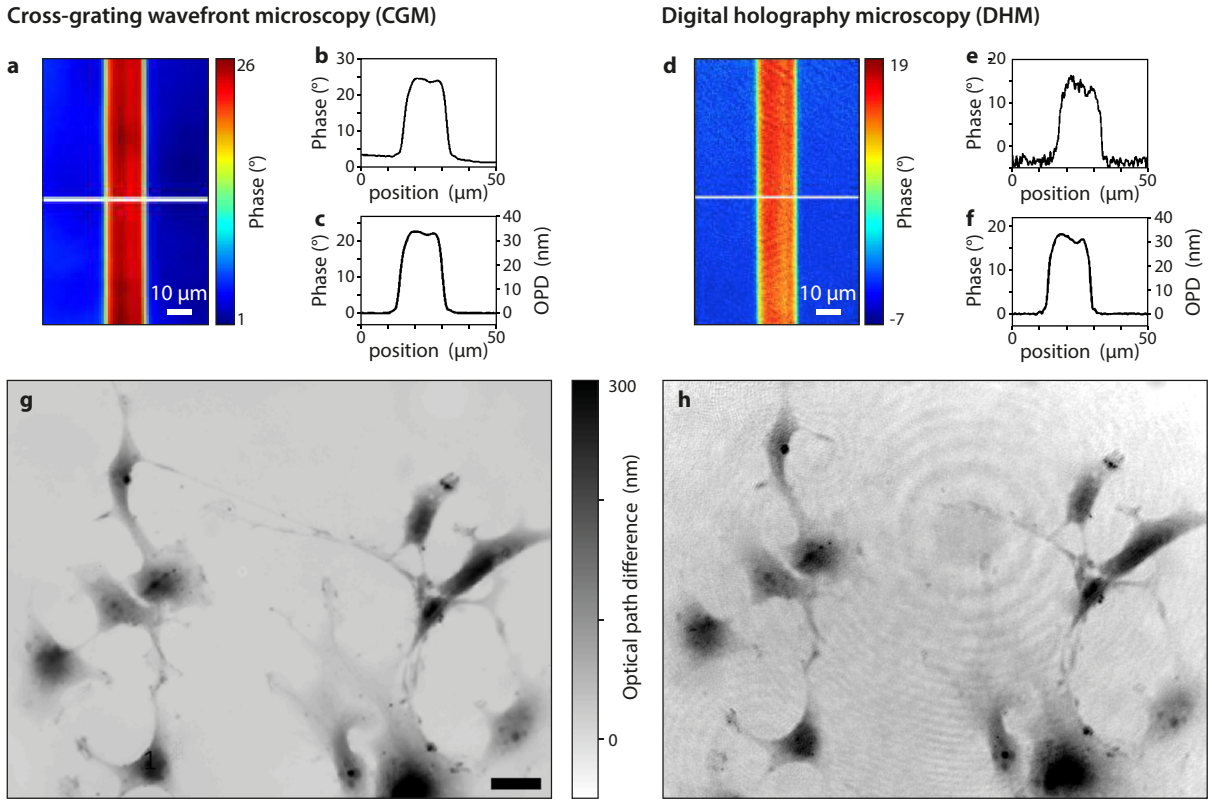

Fig. 10. (a) Phase image of a waveguide acquired using CGM, along with (b) a single line phase profile and (c) leveled phase/OPD profiles; (d) Phase image of a waveguide acquired using DHM, along with (e) a single line phase profile and (f) leveled phase/OPD profiles. Reprinted with permission from [105]. Copyright 2018 Optical Society of America. (g) OPD image of fixed COS-7 cells obtained using CGM (40×, 1.3NA) and (h) OPD image of the same cells obtained using DHM (20×, 0.7NA). Reprinted with permission from [106]. Copyright 2019 Optical Society of America.

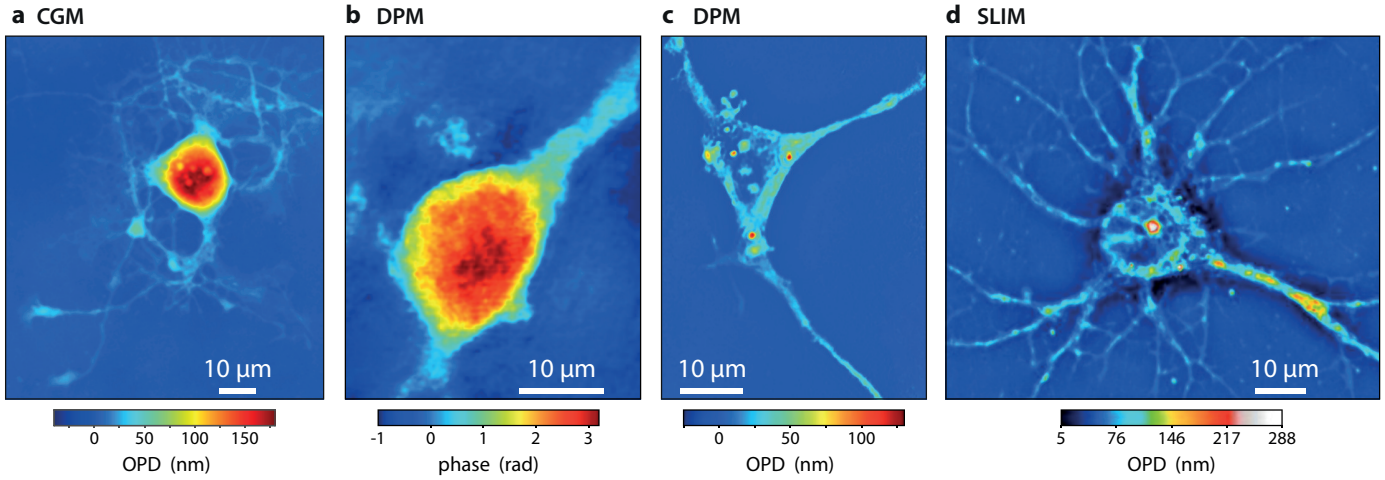

Fig. 11. OPD and phase images of neurons acquired using different techniques (a) OPD of a hippocampal neuron imaged using CGM.[45] (b) Phase image of a neuron imaged using DPM. Reprinted with permission from [6]. Copyright 2014 Optical Society of America. (c) OPD image of a neuron imaged using DPM. Reprinted with permission from [111]. Copyright 2018 Wiley. (d) OPD of a hippocampal neuron imaged using SLIM. Reprinted with permission from [7]. Copyright 2011 Optical Society of America.

nature of the measurements (OPD in nm).

No high-pass filter was applied to these images, though. Possible reasons of this mismatch can be proposed. In DPM, the size of the hole filtering the zero order is an important parameter. If it is too small, the contrast on the camera is poor. But if it is too large, the reference image (zero order) is no longer perfectly flat and can contain some low spatial frequencies. And these low spatial frequencies are subtracted to the image, which is equivalent to a high-pass filtering process. Various sizes of the filtering hole may explain why some DPM images looks consistent (Fig.

11b) and some others not (Fig. 11c).

Regarding SLIM, the underlying theory is based on the idea that any bright field image can be understood as the interference between the illuminating field U_0 and the field U_1 scattered by the imaged object. The phase profile of the light beam impinging on the camera sensor can be retrieved by applying various phase shifts between U_0 and U_1 using a spatial light modulator (SLM). However, the SLIM theory assumes that the scattered field U_1 deviates from the propagation direction of U_0, to entirely cross the phase ring. This is not always the case. For instance, when uniform areas occupy the field of view (like a uniform slab[78]), U_0 and U_1 propagate along the same path, so that the SLM cannot apply a phase shift to one field and not to the other. Besides, phase contrast only highlights boundaries of objects, not flat areas, as shown by measurements on graphene.[112] It may explain why flat areas, such as the center of the soma, display anomalous phase values close to zero using SLIM, while highly scattering areas, such as the neurites or cell edges, exhibit a strong contrast (Fig. 11d).

6. OUTLOOK

Used for long by a reduced number of educated research groups, CGM is experiencing today a large-scale dissemination in the scientific community. This Review on CGM intends to favor this dissemination by providing a comprehensive picture of the theory, the working principle, the state of the art, the community and the main driving forces and applications.

Compared with phase imaging techniques, CGM gathers important advantages: (i) It is simple (a grating in front of the camera of a regular microscope), (ii) it is potentially cost-effective due to the low number of passive optical elements to add to a standard microscope (grating and relay lens), (iii) it is high-resolution (compared with other wavefront imaging technique) and can reach the diffraction limit, (iv) it is sensitive ($0.3\ \mathrm{nm}/\sqrt{\mathrm{Hz}}$), (v) it is fast, reaching the acquisition rate of the camera used, (vi) it is weakly sensitive to external perturbations, being a common-path technique, (vii) it is achromatic (it does not require the knowledge of the wavelength) and can be used with an incoherent illumination, getting rid of fringes and speckle. (vii) The image processing algorithm is available and particularly simple, around 30 lines of code.[26, 113]

CGM, however, suffers from some limitations or difficulties: (i) CGM does not provide absolute phase values compared with a reference, because it measures wavefront gradients that are subsequently integrated to yield a wavefront image up to a constant integration value. (ii) The demodulation algorithm of CGM reduces the image definition by a factor of 3 or 4 (in each direction), which can reduce the spatial resolution. This limitation can be lifted by increasing the magnification of the microscope (at the expense of the size of the field of view) or by using camera with more pixels and smaller pixel size (at the expense of the image processing time). (iii) The grating-camera distance must be precisely known, which can be difficult to measure experimentally, especially when using a relay-lens, but which can be retrieved using calibrated samples of known OPD (like micro-grooves characterized by atomic force microscopy). (iv) QLSI gratings are not commercially available on-the-shelf yet, to our knowledge. The fabrication of a home-made CGM/QLSI system demands access to microfabrication facilities.

In the near future, one can expect CGM to spread in the microscopy community, first because the patent related to QLSI expired in 2020, and then because the community starts considering wavefront microscopy as an equally relevant technique compared with QPM,[2] which was not the case even until a few years ago. In biology, CGM should gain popularity for at least two applications: First, it can be used to easily measure dry masses of micro-organisms in a particularly simple way: CGM can be easily implemented, because it amounts to plugging a camera on an pre-existing microscope, a strong advantage compared with DHM for instance. [114, 115] Second, CGM could challenge the use of Zernike phase-contrast microscopy, a very popular microscopy technique that almost any bio-laboratory owns, but that normally consists of a separated and dedicated microscope. CGM can play the same role as phase contrast microscopy by providing highly contrasted images, but also with a strong benefit: it can be implemented on a fluorescence microscopes directly (confocal, spinning disc), enabling the characterization of the morphology of cells with high contrast on the exact same location as the cells imaged by fluorescence microscopy.

In Nanophotonics as well, e.g., for applications in plasmonics or metasurface science, CGM proved recently to be an ideal metrology tool, which could favor the dissemination of CGM due to the large size of this research community, and the need for metrology tools considering the large variety of new exotic materials being developed for the fabrication of nano- and microscale systems.

In addition to biology and nanophotonics, we envision CGM to enrich other domains of research based on optical microscopy, e.g., for the dynamical study of microscale chemistry and fluid dynamics: growth of micro-crystals, mapping of fluids mixture of various refractive indices, mapping of microscale concentration fields, or tracking of nano/microbeads as tracers in 3 dimensions.

Funding Sources

This work has received funding from the European Research Council (ERC) under the European Union's Horizon 2020 Research and Innovation Programme (grant agreement no. 772725, project HiPhore).

REFERENCES

1. Popescu, G. *Quantitative phase imaging of cells and tissues*; Mc Graw Hill, 2011.
2. Nguyen, T. L.; Pradeep, S.; Judson-Torres, R. L.; Reed, J.; Teitell, M. A.; Zangle, T. A. Quantitative Phase Imaging: Recent Advances and Expanding Potential in Biomedicine. *ACS Nano* **2022**, *16*, 11516–11544.
3. Kemper, B.; von Bally, G. Digital holographic microscopy for live cell applications and technical inspection. *Appl. Opt.* **2008**, *47*, A52–A61.
4. Marquet, P.; Depeursinge, C.; Magistretti, P. J. Review of quantitative phase-digital holographic microscopy: promising novel imaging technique to resolve neuronal network activity and identify cellular biomarkers of psychiatric disorders. *Neurophotonics* **2014**, *1*, 020901.
5. Park, Y. K.; Popescu, G.; Badizadegan, K.; Dasari, R. R.; Feld, M. S. Diffraction phase and fluorescence microscopy. *Opt. Express* **2006**, *14*, 8263–8268.
6. Bhaduri, B.; Edwards, C.; Pham, H.; Zhou, R.; Nguyen, T. H.; Goddard, L. L.; Popescu, G. Diffraction phase microscopy: principles and applications in materials and life sciences. *Adv. Opt. Photon.* **2014**, *6*, 57–119.
7. Wang, Z.; Millet, L.; Mustafa, M.; Ding, H.; Unarunotai, S.; Rogers, J.; Gillette, M. U.; Popescu, G. Spatial light interference microscopy (SLIM). *Opt Express* **2011**, *19*, 1016–1026.
8. Chen, X.; Kandel, M. E.; Popescu, G. Spatial light interference microscopy: principle and applications to biomedicine. *Adv. Opt. Photon.* **2021**, *13*, 353–425.

9. Popescu, G.; Park, Y. K.; Lue, N.; Best-Popescu, C.; Deflores, L.; Dasari, R. R.; Feld, M. S.; Badizadegan, K. Optical imaging of cell mass and growth dynamics. *Am. J. Physiol. Cell Physiol.* **2008**, *295*, C538–C544.
10. Rappaz, B.; Cano, E.; Colomb, T.; Kühn, J.; Simanis, V.; Magistretti, P. J.; Marquet, P. Noninvasive characterization of the fission yeast cell cycle by monitoring dry mass with digital holographic microscopy. *J. Biomed. Opt.* **2009**, *14*, 034049.
11. Primot, J. Three-wave lateral shearing interferometer. *Appl. Optics* **1993**, *32*, 6242.
12. Primot, J.; Guérineau, N. Extended Hartmann Test Based on the Pseudoguiding Property of a Hartmann Mask Completed by a Phase Chessboard. *Appl. Opt.* **2000**, *39*, 5715–5720.
13. Platt, B. C.; Shack, R. History and principles of Shack-Hartmann wavefront sensing. *J. Refract. Surg.* **2011**, *17*, S573–S577.
14. Primot, J. Theoretical description of Shack–Hartmann wave-front sensor. *Opt. Commun.* **2003**, *222*, 81–92.
15. Shack, R. V.; Platt, B. C. Production and use of a lenticular Hartmann screen. *J. Opt. Soc. Am.* **1971**, *61*, 656–660.
16. Forest, C. R.; Canizares, C. R.; Neal, D. R.; McGuirk, M.; Schattenburg, M. L. Metrology of thin transparent optics using Shack-Hartmann wavefront sensing. *Opt. Eng.* **2004**, *42*, 742–753.
17. Liang, J. Z.; Grimm, B.; Goelz, S.; Bille, J. F. Objective measurement of wave aberrations of the human eye with the use of a Hartmann–Shack wave-front sensor. *J. Opt. Soc. Am. A* **1994**, *11*, 1949–1957.
18. Lane, R. G.; Tallon, M. Wave-front reconstruction using a Shack-Hartmann sensor. *Appl. Opt.* **1992**, *31*, 6902–6908.
19. Andrade, P. P.; Garcia, P. J. V.; Correia, C. M.; Kolb, J.; Carvalho, M. I. Estimation of atmospheric turbulence parameters from Shack–Hartmann wavefront sensor measurements. *MNRAS* **2019**, *483*, 1192–1201.
20. Parthasarathy, A. B.; Chu, K. K.; Ford, T. N.; Mertz, J. Quantitative phase imaging using a partitioned detection aperture. *Opt. Lett.* **2012**, *37*, 4062–4064.
21. Wang, C.; Dun, X.; Fu, Q.; Heidrich, W. Ultra-high resolution coded wavefront sensor. *Opt. Express* **2017**, *25*, 13736.
22. Berto, P.; Rigneault, H.; Guillon, M. Wavefront sensing with a thin diffuser. *Opt. Lett.* **2017**, *42*, 5117–5120.
23. Wu, Y.; Sharma, K.; Veeraraghavan, A. WISH: wavefront imaging sensor with high resolution. *Light Sci. Appl.* **2019**, *8*, 44.
24. Wang, B. Y.; Han, L.; Yang, Y.; Yue, Q. Y.; Gui, C. S. Wavefront sensing based on a spatial light modulator and incremental binary random sampling. *Opt. Lett.* **2017**, *42*, 603–606.
25. Born, M.; Wolf, E. *Principles of Optics: Electromagnetic Theory of Propagation, Interference and Diffraction of Light*; Cambridge University Press, 1999.
26. Baffou, G. Quantitative phase microscopy using quadriwave lateral shearing interferometry (QLSI): principle, terminology, algorithm and grating shadow description. *J. Phys. D: Appl. Phys.* **2021**, *54*, 294002.
27. Bon, P.; Maucort, G.; Wattellier, B.; Monneret, S. Quadriwave lateral shearing interferometry for quantitative phase microscopy of living cells. *Opt Express* **2009**, *17*, 13080–94.
28. Primot, J.; Guérineau, N. Achromatic optical interferometer with continuously adjustable sensitivity. *Patent* **2000**, 6577403.
29. Marthy, B.; Baffou, G. Cross-grating phase microscopy (CGM): In silico experiment (insilex) algorithm, noise and accuracy. *Opt. Commun.* **2022**, *521*, 128577.
30. Velghe, S.; Primot, J.; Guérineau, N.; Cohen, M.; Wattellier, B. Wavefront Reconstruction from Multidirectional Phase Derivatives Generated by Multilateral Shearing Interferometers. *Opt. Lett.* **2005**, *30*, 245–247.
31. Primot, J.; Sogno, L. Achromatic three-wave (or more) lateral shearing interferometer. *J. Opt. Soc. Am. A* **1995**, *12*, 2679.
32. Peng, C.; Tang, F.; Wang, X.; Li, J. Circular-aperture Modified Hartmann Mask for quadriwave lateral shearing interferometry. *Opt. Commun.* **2019**, *451*, 86–96.
33. Patorski, K.; Służewski, Ł.; Trusiak, M. 5-beam grating interferometry for extended phase gradient sensing. *Opt. Express* **2018**, *26*, 26872–26887.
34. Li, Y.; Zhang, J.; Li, J. Generation and Evolution of Vortex Array with Variable-ratio Lateral-shearing Interferometry. *J. Opt.* **2022**, accepted manuscript.
35. Ling, T.; Liu, D.; Yue, X.; Yang, Y.; Shen, Y.; Bai, J. Quadriwave lateral shearing interferometer based on a randomly encoded hybrid grating. *Opt. Lett.* **2015**, *40*, 2245.
36. Wang, C.; Fu, Q.; Dun, X.; Heidrich, W. Quantitative phase and intensity Microscopy Using Snapshot White Light Wavefront Sensing. *Sci. Rep.* **2019**, *9*, 13795.
37. Wu, T.; Guillon, M.; Gentner, C.; Rigneault, H.; Tessier, G.; Bon, P.; Berto, P. 3D nanoparticle superlocalization with a thin diffuser. *Opt. Lett.* **2022**, *47*, 3079–3082.
38. Brasiliense, V.; Audibert, J. F.; Wu, T.; Tessier, G.; Berto, P.; Miomandre, F. Local Surface Chemistry Dynamically Monitored by Quantitative Phase Microscopy. *Small Methods* **2022**, *6*, 2100737.
39. Bon, P.; Lécart, S.; Fort, E.; Lévêque-Fort, S. Fast Label-Free Cytoskeletal Network Imaging in Living Mammalian Cells. *Biophys. J.* **2014**, *106*, 1588–1595.
40. Aknoun, S.; Savatier, J.; Bon, P.; Galland, F.; Abdeladim, L.; Wattellier, B.; Monneret, S. Living cell dry mass measurement using quantitative phase imaging with quadriwave lateral shearing interferometry: an accuracy and sensitivity discussion. *J. Biomed. Opt.* **2015**, *20*, 126009.
41. Berto, P.; Philippet, L.; Osmond, J.; Liu, C. F.; Afridi, A.; Montagut Marques, M.; Molero Agudo, B.; Tessier, G.; Quidant, R. Tunable and Free-Form Planar Optics. *Nat. Photonics* **2019**, *13*, 649–656.
42. Khadir, S.; Andrén, D.; Verre, R.; Song, Q.; Monneret, S.; Genevet, P.; Käll, M.; Baffou, G. Metasurface optical characterization using quadriwave lateral shearing interferometry. *ACS Photonics* **2021**, *8*, 603–613.
43. Liu, X.; Oh, S.; Peshkin, L.; Kirschner, M. W. Computationally enhanced quantitative phase microscopy reveals autonomous oscillations in mammalian cell growth. *Proc. Natl. Acad. Sci.* **2020**, *117*, 27388–27399.
44. Pradeep, S.; Tasnmin, T.; Zhang, H.; Zangle, T. A. Simultaneous measurement of neurite and neural body mass accumulation via quantitative phase imaging. *Analyst* **2021**, *146*, 1361.
45. Durdevic, L.; Relaño Gines, A.; Roueff, A.; Blivet, G.; Baffou, G. Biomass measurements of single neurites in vitro using optical wavefront microscopy. *Biomed. Opt. Express* **2022**, *13*, 6550–6560.
46. Pradeep, S.; Zangle, T. A. Quantitative phase velocimetry measures bulk intracellular transport of cell mass during the cell cycle. *Sci. Rep.* **2022**, *12*, 6074.
47. Robert, H. M. L.; Savatier, J.; Vial, S.; Verghese, J.; Wattellier, B.; Rigneault, H.; Monneret, S.; Polleux, J.; Baffou, G. Photothermal Control of Heat-shock Protein Expression at the Single Cell Level. *Small* **2018**, *14*, 1801910.
48. Molinaro, C.; Bénéfice, M.; Gorlas, A.; Da Cunha, V.; Robert, H. M. L.; Catchpole, R.; Gallais, L.; Forterre, P.; Baffou, G. Life at high temperature observed in vitro upon laser heating of gold nanoparticles. *Nat. Commun.* **2022**, *13*, 5342.
49. Aknoun, S.; Aurrand-Lions, M.; Wattellier, B.; Monneret, S. Quantitative retardance imaging by means of quadri-wave lateral shearing interferometry for label-free fiber imaging in tissues. *Opt. Commun.* **2018**, *422*, 17–27.
50. Bon, P.; Cognet, L. On Some Current Challenges in High-Resolution Optical Bioimaging. *ACS Photonics* **2022**, *9*, 2538–2546.
51. Bon, P.; Savatier, J.; Merlin, M.; Wattellier, B.; Monneret, S. Optical detection and measurement of living cell morphometric features with single-shot quantitative phase microscopy. *J. Biomed. Opt.* **2012**, *17*, 076004.
52. Barer, R. Interference Microscopy and Mass Determination. *Nature* **1952**, *169*, 366.
53. Zangle, T. A.; Teit, Live-cell mass profiling: an emerging approach in quantitative biophysics. *Nat. Methods* **2014**, *11*, 1221–1228.
54. Aknoun, S.; Yonnet, M.; Djabari, Z.; Graslin, F.; Taylor, M.; Pourcher, T.; Wattellier, B.; Pognonec, P. Quantitative phase microscopy for non-invasive live cell population monitoring. *Sci. Rep.* **2021**, *11*, 4409.
55. Ohene, Y.; Marinov, I.; de Laulanié, I.; Dupuy, C.; Wattellier, B.; Starikovskaia, S. Phase imaging microscopy for the diagnostics of plasma-cell interaction. *Appl. Phys. Lett.* **2015**, *106*, 233703.

56. Zlotek-Zlotkiewicz, E.; Monnier, S.; Cappello, G.; M., L. B.; Piel, M. Optical volume and mass measurements show that mammalian cells swell during mitosis. *J. Cell Biol.* **2017**, *211*, 765–774.
57. Llinares, J.; Cantereau, A.; Froux, L.; Becq, F. Quantitative phase imaging to study transmembrane water fluxes regulated by CFTR and AQP3 in living human airway epithelial CFBE cells and CHO cells. *PLoS One* **2020**, *29*, e0233439.
58. Murray, G. F.; Guest, D.; Mikheykin, A.; Toor, A.; Reed, J. Single cell biomass tracking allows identification and isolation of rare targeted therapy-resistant DLBCL cells within a mixed population. *Analyst* **2021**, *146*, 1157–1162.
59. Kim, G.; Ahn, D.; Park, J.; Ryu, D.; Jo, Y.; Song, J.; Sung, J., Ryu; Choi, G.; Ryeon Chung, D.; Young Yoo, I.; Jae Huh, H.; Min, H. S.; N., Y. L.; Park, Y. K. Rapid species identification of pathogenic bacteria from a minute quantity exploiting three-dimensional quantitative phase imaging and artificial neural network. *Light Sci. Appl.* **2022**, *11*, 190.
60. Girshovitz, P.; Shaked, N. T. Generalized cell morphological parameters based on interferometric phase microscopy and their application to cell life cycle characterization. *Biomed. Opt. Express* **2012**, *3*, 1757.
61. Kim, D. N. H.; Lim, A. A.; Teitell, M. A. Rapid, label-free classification of tumor-reactive T cell killing with quantitative phase microscopy and machine learning. *Sci. Rep.* **2021**, *11*, 19448.
62. Pezhouman, A.; Nguyen N. B. and, A. J., Sercel; Nguyen, T. L.; Daraei, A.; Sabri, S.; Chapski, D. J.; Zheng, M.; Patananan, A. N.; Ernst, J.; K., P.; Vondriska, T. M.; Teitell, M. A.; Ardehali, R. Transcriptional, Electrophysiological, and Metabolic Characterizations of hESC-Derived First and Second Heart Fields Demonstrate a Potential Role of TBX5 in Cardiomyocyte Maturation. *Front. Cell Dev. Biol.* **2021**, *9*, 787684.
63. Aknoun, S.; Bon, P.; Savatier, J.; Wattellier, B.; Monneret, S. Quantitative retardance imaging of biological samples using quadriwave lateral shearing interferometry. *Opt. Express* **2015**, *23*, 16383–16406.
64. Boccara, A. C.; Fournier, D.; Badoz, J. Thermooptical Spectroscopy: Detection by the "mirage effect". *Appl. Phys. Lett.* **1980**, *36*, 130–132.
65. Jackson, W. B.; Amer, N. M.; Boccara, A. C.; Fournier, D. Photothermal Deflection Spectroscopy and Detection. *Appl. Opt.* **1981**, *20*, 1333–1344.
66. Fournier, D.; Lepoutre, F.; Boccara, A. Tomographic Approach for Photothermal Imaging Using the Mirage Effect. *J. Phys. Coll.* **1983**, *44*, C6–479–C6–482.
67. Baffou, G.; Bon, P.; Savatier, J.; Polleux, J.; Zhu, M.; Merlin, M.; Rigneault, H.; Monneret, S. Thermal Imaging of Nanostructures by Quantitative Optical Phase Analysis. *ACS Nano* **2012**, *6*, 2452–2458.
68. Quintanilla, M.; Liz-Marzán, L. M. Guiding Rules for Selecting a Nanothermometer. *Nano Today* **2018**, *19*, 126–145.
69. Baffou, G.; Rigneault, H.; Marguet, D.; Jullien, L. A Critique of Methods for Temperature Imaging in Single Cells. *Nat. Methods* **2014**, *11*, 899–901.
70. Kiyonaka, S.; Sakaguchi, R.; Hamachi, I.; Morii, T.; Yoshizaki, T.; Mori, Y. Validating subcellular thermal changes revealed by fluorescent thermosensors. *Nat. Methods* **2015**, *12*, 801–802.
71. Suzuki, M.; Zeeb, V.; Arai, S.; Oyama, K.; Ishiwata, S. The 10^5 gap issue between calculation and measurement in single-cell thermometry. *Nat. Methods* **2014**, *12*, 802–803.
72. Baffou, G.; Rigneault, H.; Marguet, D.; Jullien, L. Reply to: "Validating Subcellular Thermal Changes Revealed by Fluorescent Thermosensors" and "The 10^5 Gap Issue Between Calculation and Measurement in Single-Cell Thermometry". *Nat. Methods* **2015**, *12*, 803.
73. Baffou, G.; Polleux, J.; Rigneault, H.; Monneret, S. Super-Heating and Micro-Bubble Generation around Plasmonic Nanoparticles under cw Illumination. *J. Phys. Chem. C* **2014**, *118*, 4890.
74. Zhu, M.; Baffou, G.; Meyerbröker, N.; Polleux, J. Micropatterning Thermoplasmonics Gold Nanoarrays to Manipulate Cell Adhesion. *ACS Nano* **2012**, *6*, 7227–7233.
75. Oh, J. T.; Lee, G. H.; Rho, J.; Shin, S.; Jae Lee, B.; Nam, Y.; Park, Y. K. Optical Measurements of Three-Dimensional Microscopic Temperature Distributions Around Gold Nanorods Excited by Localized Surface Plasmon Resonance. *Phys. Rev. A* **2019**, *11*, 044079.
76. Ciraulo, B.; Garcia-Guirado, J.; de Miguel, I.; Ortega Arroyo, J.; Quidant, R. Long-range optofluidic control with plasmon heating. *Nat. Commun.* **2021**, *12*, 2001.
77. Bon, P.; Bourg, N.; Lécart, S.; Monneret, S.; Fort, E.; Wenger, J.; Léveque-Fort, S. Three-Dmensional Nanometre Localization of Nanoparticles to Enhance Super-Resolution Microscopy. *Nat. Commun.* **2015**, *6*, 7764.
78. Khadir, S.; Bon, P.; Vignaud, D.; Galopin, E.; McEvoy, N.; McCloskey, D.; Monneret, S.; Baffou, G. Optical Imaging and Characterization of Graphene and Other 2D Materials Using Quantitative Phase Microscopy. *ACS Photonics* **2017**, *4*, 3130–3139.
79. Song, Q.; Khadir, S.; Vézian, S.; Damilano, B.; de Mierry, P.; Chenot, S.; Brandli, V.; Labardesque, R.; Wattellier, B.; Genevet, P. Printing polarization and phase at the optical diffraction limit: near- and far-field optical encryption. *Nanophotonics* **2021**, *10*, 697–704.
80. Bon, P.; Linarès-Loyez, J.; Feyeux, M.; Alessandri, K.; Lounis, B.; Nassoy, P.; Cognet, L. Self-interference 3D super-resolution microscopy for deep tissue investigations. *Nat. Methods* **2018**, *15*, 449–454.
81. Baffou, G.; Quidant, R. Thermo-plasmonics: Using Metallic Nanostructures as Nano-Sources of Heat. *Laser Photonics Rev.* **2013**, *7*, 171–187.
82. Baffou, G.; Cichos, F.; Quidant, R. Applications and challenges of thermoplasmonics. *Nat. Mater.* **2020**, *19*, 946 – 958.
83. Jauffred, L.; Samadi, A.; Klingberg, H.; Bendix, P. M.; Oddershede, L. B. Plasmonic heating of nanostructures. *Chem. Rev.* **2019**, *119*, 8087–8130.
84. Bon, P.; Belaid, N.; Lagrange, D.; Bergaud, C.; Rigneault, H.; Monneret, S.; Baffou, G. Three-dimensional temperature imaging around a gold microwire. *Appl. Phys. Lett.* **2013**, *102*, 244103.
85. Robert, H. M. L.; Kundrat, F.; Bermúdez Ureña, E.; Rigneault, H.; Monneret, S.; Quidant, R.; Polleux, J.; Baffou, G. Light-Assisted Solvothermal Chemistry Using Plasmonic Nanoparticles. *ACS Omega* **2016**, *1*, 2–8.
86. Baffou, G.; Bermúdez Ureña, E.; Berto, P.; Monneret, S.; Quidant, R.; Rigneault, H. Deterministic Temperature Shaping using Plasmonic Nanoparticle Assemblies. *Nanoscale* **2014**, *6*, 8984–8989.
87. Durdevic, L.; Robert, H. M. L.; Wattellier, B.; Monneret, S.; Baffou, G. Microscale Temperature Shaping Using Spatial Light Modulation on Gold Nanoparticles. *Sci. Rep.* **2019**, *9*, 4644.
88. Liu, C.; Tessier, G.; Esparza, S. I. F.; Guillon, M.; Berto, P. Reconfigurable Temperature Control at the Microscale by Light Shaping. *ACS Photonics* **2019**, *6*, 422–428.
89. Shakib, S.; Rogez, B.; Khadir, S.; Polleux, J.; Würger, A.; Baffou, G. Microscale Thermophoresis in Liquids Induced by Plasmonic Heating and Characterized by Phase and Fluorescence Microscopies. *J Phys Chem C* **2021**, *125*.
90. Khadir, S.; Andrén, D.; Chaumet, P. C.; Monneret, S.; Bonod, N.; Käll, M.; Sentenac, A.; Baffou, G. Full optical characterization of single nanoparticles using quantitative phase imaging. *Optica* **2020**, *7*, 243–248.
91. Khadir, S.; Chaumet, P. C.; Baffou, G.; Sentenac, A. Quantitative model of the image of a radiating dipole through a microscope. *Journal of the Optical Society of America A* **2019**, *36*, 478–484.
92. Wenger, J.; Bon, P.; Monneret, S. Three-dimensional focusing device and method for a microscope. *US Patent* **2014**, US10261305B2.
93. Linarès-Loyez, J.; Ferreira, J. S.; Rossier, O.; Lounis, B.; Giannone, G.; Groc, L.; Cognet, L.; Bon, P. Self-interference (SELFI) Microscopy for Live Super-Resolution Imaging and Single Particle Tracking in 3D. *Front. Phys.* **2019**, *7*, 68.
94. Saemisch, L.; van Hulst, N. F.; Liebel, M. One-shot phase image distinction of plasmonic and dielectric nanoparticles. *Nano Lett.* **2021**, *21*, 4021–4028.
95. Liebel, M.; Camargo, F. V. A.; Cerullo, G.; van Hulst, N. F. Ultrafast transient holography microscopy. *Nano Lett.* **2021**, *21*, 1666–1671.
96. Ortiz-Orruño, U.; Jo, A.; van Hulst, N. F.; Liebel, M. Precise nanosizing with high dynamic range holography. *Nano Lett.* **2021**, *21*, 317–322.
97. Genevet, P.; Capasso, F.; Aieta, F.; Khorasaninejad, M.; R., D. Recent advances in planar optics: from plasmonic to dielectric metasurfaces.

Optica **2017**, *4*, 139–152.
98. Douti, D. B. L.; Chrayteh, M.; Aknoun, S.; Doualle, T.; Hecquet, C.; Monneret, S.; Gallais, L. Quantitative phase imaging applied to laser damage detection and analysis. *Appl. Opt.* **2015**, *54*, 8375–8382.
99. Gallais, L.; Monneret, S. Time-resolved quantitative-phase microscopy of laser-material interactions using a wavefront sensor. *Opt. Lett.* **2016**, *41*, 3245–3248.
100. Doualle, T.; Gallais, L.; Monneret, S.; Bouillet, S.; Bourgeade, A.; Ameil, C.; Lamaignère, L.; Cormont, P. CO_2 laser microprocessing for laser damage growth mitigation of fused silica optics. *Opt. Eng.* **2017**, *56*, 011022.
101. Doualle, T.; Ollé, A.; Cormont, P.; Monneret, S.; Gallais, L. Laser-induced birefringence measurements by quantitative polarized-phase microscopy. *Opt. Lett.* **2017**, *42*, 1616.
102. Radhakrishnan, R.; Gallais, L.; Monneret, S. Wavefront sensing applied to determine the temperature dependence of the refractive index of liquids. *Appl. Opt.* **2019**, *58*, 3646–3651.
103. Marquet, P.; Rappaz, B.; Magistretti, P. J.; Cuche, E.; Emery, Y.; Colomb, T.; Depeursinge, C. Digital holographic microscopy: a noninvasive contrast imaging technique allowing quantitative visualization of living cells with subwavelength axial accuracy. *Opt. Lett.* **2005**, *30*, 468–470.
104. Emery, Y.; Colomb, T.; Cuche, E. Metrology applications using off-axis digital holography microscopy. *J. Phys.: Photon.* **2021**, *3*, 034016.
105. Bélanger, E.; Bérubé, J. P.; de Dorlodot, B.; Marquet, P.; Vallée, R. Comparative study of quantitative phase imaging techniques for refractometry of optical waveguides. *Opt. Express* **2018**, *26*, 17498–17511.
106. Allier, C.; Hervé, L.; Mandula, O.; Blandin, P.; Usson, Y.; Savatier, J.; Monneret, S.; Morales, S. Quantitative phase imaging of adherent mammalian cells: a comparative study. *Biomed. Opt. Express* **2019**, *10*, 2768–2783.
107. Gentner, C.; Kuszelewicz, R.; Berto, P.; Hkelfa, H.; Tessier, G. Viscosity imaging using heterodyne holographic spectral analysis of Brownian nanorod rotation. *Opt. Express* **2021**, *29*, 527–537.
108. Wu, T.; Berto, P.; Guillon, M. Reference-less complex wavefields characterization with a high-resolution wavefront sensor. *Appl. Phys. Lett.* **2021**, *118*, 251102.
109. Ling, T.; Boyle, K. C.; Zuckerman, V.; Flores, T.; Ramakrishnan, C.; Deisseroth, K.; Palanker, D. High-speed interferometric imaging reveals dynamics of neuronal deformation during the action potential. *Proc. Natl. Acad. Sci.* **2020**, *117*, 10278–10285.
110. Wang, Z.; Chun, I. S.; Li, X.; Ong, Z. Y.; Pop, E.; Millet, L.; Gilette, M.; Popescu, G. Topography and Refractometry of Nanostructures Using Spatial Light Interference Microscopy. *Opt. Lett.* **2010**, *35*, 208–210.
111. Hu, C.; Sam, R.; Mingguang, M.; Shan, M.; Nastasa, V.; Wang, M.; Kim, T.; Gillette, M.; Sengupta, P.; Popescu, G. Optical excitation and detection of neuronal activity. *J. Biophotonics* **2019**, *12*, e201800269.
112. Wang, X.; Chen, Y. P.; Nolte, D. D. Strong anomalous optical dispersion of graphene: complex refractive index measured by Picometrology. *Opt Express* **2008**, *16*, 22105.
113. Baffou, G. https://github.com/baffou/CGMprocess.
114. Cacace, T.; Bianco, V.; Ferraro, P. Quantitative phase imaging trends in biomedical applications. *Opt. Lasers Eng.* **2020**, *135*, 106188.
115. Park, Y. K.; Depeursinge, C.; Popescu, G. Quantitative phase imaging in biomedicine. *Nat. Photonics* **2018**, *12*, 578–589.